minerals

MDPI

Article

Fe–Ti(–V) Oxide Deposits of the Kunene Anorthosite Complex (SW Angola): Mineralogy and Thermo-Oxybarometry

Cristina Villanova-de-Benavent [1,*], Lisard Torró [1], Montgarri Castillo-Oliver [2], Marc Campeny [1,3], Joan Carles Melgarejo [1], Xavier Llovet [4], Salvador Galí [1] and Antonio Olimpio Gonçalves [5]

1 Departament de Mineralogia, Petrologia i Geologia Aplicada, Facultat de Geologia, Universitat de Barcelona, Martí i Franquès s/n, 08028 Barcelona, Spain; lisardtorro@hotmail.com (L.T.); mcampenyc@bcn.cat (M.C.); joan.carles.melgarejo.draper@ub.edu (J.C.M.); gali@ub.edu (S.G.)

2 ARC Centre of Excellence for Core to Crust Fluid Systems and GEMOC, Department of Earth and Planetary Sciences, Macquarie University, Sydney, NSW 2019, Australia; montgarri.castillo-oliver@mq.edu.au

3 Departament de Mineralogia, Museu de Ciències Naturals de Barcelona, Pg. Picasso s/n, 08003 Barcelona, Spain

4 Centres Científics i Tecnològics, Universitat de Barcelona, Lluís Solé i Sabarís, 1-3, 08028 Barcelona, Spain; xavier@ccit.ub.edu

5 Departamento de Geologia, Universidade Agostinho Neto, Av. 4 de Fevereiro 71, 815 Luanda, Angola; tonygoncalves72@hotmail.com

* Correspondence: cvillanovadb@ub.edu or cvillanovadb@gmail.com; Tel.: +34-93-402-1341

Received: 25 October 2017; Accepted: 12 December 2017; Published: 14 December 2017

Abstract: The Kunene Intrusive Complex (KIC), in NW Namibia and SW Angola, is one of the largest Proterozoic anorthosite massif-type exposures in the world. A geochemical, mineralogical and petrological study of four Fe–Ti(–V) oxide bodies located in the understudied Angolan part of the KIC has been performed. The massive Fe–Ti(–V) oxide bodies, locally apatite-rich (nelsonites), are lenticular or dike-like. They consist mostly of titaniferous magnetite, ilmenite and minor aluminous spinel, apatite, olivine and graphite. Titaniferous magnetite displays a wide variety of subsolvus features, including aluminous spinel–magnetite–ulvöspinel exsolutions and ilmenite (Trellis) exsolutions. This work estimated the composition of the titaniferous magnetite prior to the exsolution, in order to calculate the temperature and oxygen fugacity of the different lithologies of each ore body. The thermo-oxybarometry results obtained range from 600 °C to 820 °C and fO_2 from $10^{-24.7}$ to $10^{-14.7}$. These values do not correspond to magmatic crystallization in equilibrium, but to a later re-equilibration. In addition, the mineralogical and geochemical results indicate that the studied ore bodies contain economic reserves of Ti, V, and possibly of P and REE.

Keywords: titaniferous magnetite; ilmenite; exsolution; nelsonite; massif-type anorthosite; Fe–Ti oxide thermometry

1. Introduction

Magmatic Fe–Ti(–V) oxide deposits associated with anorthosites are major sources of Ti [1,2]. At present, three active mines that beneficiate magmatic Ti ores (Tellnes, Lac Tio and Damiao) account for no less than 30% of the world's production of this metal [3]. In addition, vanadium is a common byproduct (usually below 0.2% V) [4]. These deposits occur as massive oxide bands embracing some hundreds of million tons of ore with a mineralogy dominated by ilmenite and titaniferous magnetite [4–6]. Andesine ($An_{23–48}$) anorthosites are described to contain the most important magmatic Fe–Ti oxide ores, even if significant resources are described also for labradorite

($An_{45–63}$) anorthosites [6]. The latter, on the other hand, may be associated with abundant apatite mineralization crystallized from nelsonitic magmas that may represent economic resources of P and rare-earth elements (REE) [4,7].

The Kunene Intrusive Complex (KIC), located in SW Angola and NW Namibia, is one of the largest occurrences of anorthositic rocks in the world, cropping out with an approximated area of 18.000 km^2 [8,9].

Anorthosites and other related rocks of the KIC have been extensively studied in the Namibian part [10–13], when compared to the Angolan part [8,14]. Geologic mapping was developed in Angola by the Portuguese during the colonization in the 1960's, which revealed several Fe–Ti oxide massive bodies [15,16], as well as related Fe–Ti oxide alluvial concentrations [17]. Since then, the difficult sociopolitical situation in Angola had prevented fieldwork in the area and later studies were largely based on old samplings [18–22]. Therefore, in the Angolan part of the KIC, textural and chemical information on the Fe–Ti oxide mineralizations is very sparse [16,23–25].

The present work is based on a recent, thorough sampling of four Fe–Ti(–V) oxide intrusive bodies, located in the Angolan part of the KIC (Dongue Sul, Tchingunguanganda, Tchimbueio and Chiange Velho). The aim of this contribution is to describe the structure and mineralogy of these Fe–Ti(–V) ore deposits and to provide an approximation to their genesis conditions and their evolutive history based on the interpretation of their mineralogy, textures and Fe–Ti oxide thermo-oxybarometric calculations.

2. Geological Setting

The KIC has been historically classified into a variety of typologies, namely: (i) A massif-type complex [24,26,27]; (ii) a stratified intrusion [21,28]; (iii) a combination of both [10,18] or (iv) a composite complex [8,15]. However, recent literature agrees on the origin of the KIC as a massif-type anorthosite, composed of several individual plutons, both in the Angolan and the Namibian part of the KIC [9,11–13,29,30]. In particular, reference [8] identified up to twelve individual anorthosite bodies, all with different shapes, color and either presence or absence of planar structures.

The KIC was emplaced near the southern margin of the Congo Craton [8,21] and is mainly composed of anorthosites, leucotroctolites and troctolites, with minor gabbros and norites [8,18,22]. Massive anorthosites contribute about 90% by volume to the KIC and mostly preserve igneous textures, apparently with absence of metamorphic overprint [29].

The basement in the southern KIC is the Epupa Complex, which consists of two distinct metamorphic units [31,32]: (i) The granulite facies metasediments, charnockites and metabasites of the Epembe Unit (affected by ultra-high temperature metamorphism at 1450 ± 50 Ma [31,33]); and (ii) the metasediments, amphibolites and granitic gneisses of the Orue Unit (affected by upper-amphibolite facies metamorphism and partial melting at ca. 1340–1320 Ma [32,34]). The low-pressure granulite facies metasediments exposed along the Kunene river were intruded by metagranites and granites with early Palaeoproterozoic (ca. 1800 Ma) and Mesoproterozoic (1530–1520 Ma) emplacement ages [35]. In contrast, the northern KIC is partially hosted by the so-called regional granite (Figure 1) and by various leucogranitoid units. The regional granite is equigranular and biotite-rich, with ages spanning almost the entire Eburnean period: From 1847 ± 62 Ma to 2243 ± 49 Ma (Rb-Sr whole rock [20,36]). The leucogranitoids dated yield an age of 1761 ± 19 Ma [37].

The contact between the complex and the metamorphic basement are usually obliterated by wide ductile shear belts and later brittle faults, except in some localities, where the anorthosite is exposed in contact with the garnet–cordierite–sillimanite hornfels of the Orue unit [30]. According to [8,9,29], the Kunene Complex did not experience any kind of prograde metamorphism after its emplacement, evidenced by the preservation of magmatic textures widespread in the KIC [9], unlike most of anorthositic bodies in the world. However, whole rock K-Ar ages of approximately 2100 Ma, 1300 Ma, 1000 Ma and 500 Ma were interpreted as the result of Eburnean, Kibaran and Pan-African metamorphism on the KIC [20]. Finally, at the eastern side, between 10% and 15% of the KIC is covered by the Pliocene-Quaternary alluvial sediments of the Kalahari Unit [8,9] (Figure 1).

The KIC consists of two parts separated by a set of elongated, granitic bodies [9]. The northern part, elongated N–S, is dominated by massive, slightly weathered anorthosites and leucotroctolites [12,38]. In contrast, the southern part is elongated E–W and formed by a massive body of strongly altered, coarse-grained pale anorthosite (referred to as "white anorthosite" in [11,12]) and a layered body of pale and dark anorthosites and leucotroctolites [11,12]. Dikes and sills of the dark anorthosite intruded pale anorthosite, and contain xenoliths of the latter. Plagioclase from the northern KIC anorthosites has an average composition of 70 ± 5% normative An [9], whereas the southern one is $An_{43–53}$ (white anorthosite) and $An_{43–75}$ (dark anorthosite) [12].

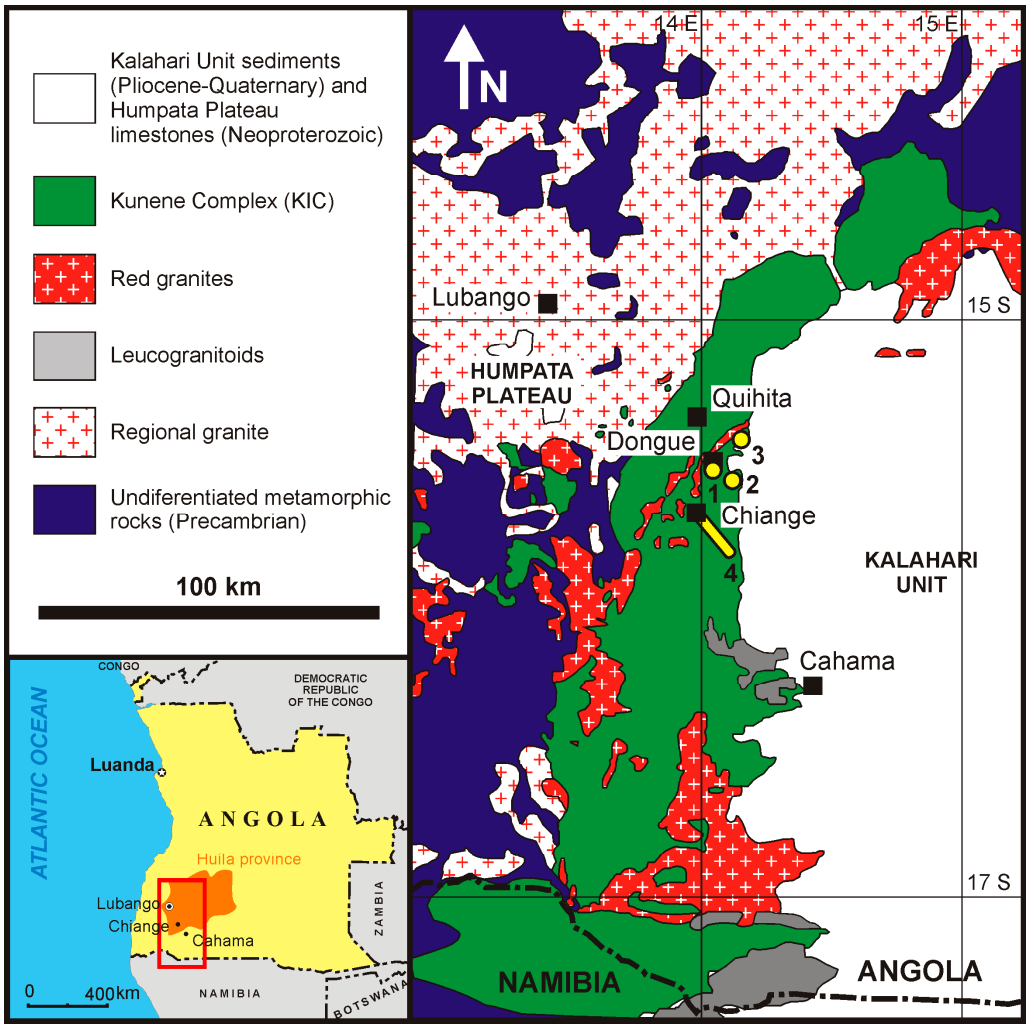

Figure 1. Simplified geological map of the Kunene Complex in SW Angola (modified from [9]), indicating the location of the four Fe–Ti(–V) oxide occurrences studied in the present paper: Dongue Sul (1), Tchimbueio (2), Tchingunguanganda (3) and Chiange Velho (4).

In the Angolan part (Figure 1), anorthosites are composed by centimetric to decimetric plagioclase crystals, with a composition of $An_{48–70}$, which are set in a pseudo-ophitic matrix of olivine and orthopyroxene [9]. The magmatic texture is clearly preserved. Weak laminations concentrated in bands of centimetric width and hectometric length can be observed locally. This anisotropy, supposed to be syn-magmatic, is defined by the preferred orientation of plagioclase crystals in non-oriented intercumulus mafic minerals [9]. Dolerite and basaltic dikes associated with the anorthosites may present a well-defined magmatic layering parallel to the contact, so they may be cogenetic with the KIC [39]. There is also a mangerite vein near the locality of Dongue Sul, which has been interpreted

as contemporary with the anorthosite [9]. Furthermore, mafic and ultramafic bodies are found in the periphery of the KIC, with a composition ranging from dunite to harzburgite, pyroxenite, troctolite, gabbro and anorthosite, and possibly constitute satellites to the KIC. These mafic and ultramafic bodies contain Ni-rich sulfides with up to 3–4% Ni, massive chromitites and low PGE concentrations, less than 25 ppb [10,27,28,30,38]. These basic and ultrabasic bodies may be mantle-derived, related to thermal activity during a rifting episode, but they are also interpreted as co-magmatic with the KIC [38]. In connection with this basic magmatism stage, acidic intrusives were emplaced crosscutting the KIC in different places. Because of meteorization, they acquired a characteristic reddish color, so that they are known as "red granites" [9]. This group of rocks includes granites, monzonites, syenites, charnockites, mangerites and rhyolitic porphyries [18]. Structural relations between these acidic bodies and the anorthosites show that granites are younger or contemporary. According to [40], these granites may represent crustal melts developed through heating by basaltic magmas emplaced at depth, whereas [9,12] advocate for crustal anatexis, as suggested by the wide range of $(^{87}Sr/^{86}Sr)_o$ ratios.

The age of the complex has been constrained within the Grenville–Kibaran cycle. Already deduced by [18] from field observations, and confirmed by K-Ar plagioclase dating of the northern KIC, the complex yields pre-Eburnean ages [9]. In the northern Angolan part, the anorthosites have been dated at 1343 ± 13 Ma (whole-rock Rb-Sr method; [39]). The southern KIC has been dated at 1408–1470 Ma from gneisses metamorphosed by the intrusion of the complex (U-Pb in zircons, [20]) and a "dark anorthosite" leucogabbronorite from the Namibian part yielded an age of 1385 ± 25 Ma (U-Pb in zircons; [41]). A more precise emplacement age of the main KIC anorthosite complex is 1363 ± 17 Ma (Pb-Pb in baddeleyite from the complex, [30]). The associated felsic rocks give 1371 ± 2.5 Ma (U-Pb in zircons from a cogenetic mangerite vein in the Angolan part [9,12]) and 1376 ± 2 Ma (U-Pb in zircons from the syenite suite of the Namibian part [12]). Therefore, the emplacement of the anorthosite and the felsic suites took place during the same igneous event [12]. These ages coincide with most Proterozoic anorthositic massif-type occurrences [21]. Furthermore, the red granites were dated by several authors [19,36,42,43] by Rb-Sr whole-rock isochrones. Their ages vary from 1302 ± 20 Ma to 1411 ± 24 Ma (Rb-Sr whole-rock isochrons) so they formed during the early Kibaran [36]. According to [9], this represents the minimum age of the KIC, because these bodies are younger or synchronous to the complex.

Massive Fe–Ti oxide and nelsonite (apatite-Fe–Ti oxide rocks) bodies are frequent in the KIC, especially near the granitic belt (Figure 1) [9,14,27,30,44–46]. Anorthosites in contact with these mineralizations contain moderate quantities of poikilitic ilmenite and/or magnetite centimetric crystals, suggesting a genetic relationship between anorthosites and oxide ore bodies [9].

2.1. Structure of the Fe–Ti(–V) Oxide Bodies

Four Fe–Ti(–V) oxide bodies located at the Huíla province, in SW Angola were studied (Figure 1): (a) Dongue Sul (Figure 2a–e); (b) Tchimbueio (Figure 2f,g); (c) Tchingunguanganda (Figure 2h,i) and (d) Chiange Velho (Figure 2j–l). These bodies crosscut the regional NE–SW foliation of the anorthosites. The Fe–Ti oxide rocks are more resistant to weathering than the surrounding host anorthosites, giving rise to metric to decametric positive reliefs (i.e., Figure 2c,f,h).

2.1.1. Dongue Sul

Dongue Sul, 1300 m to the south of Dongue (Figures 1 and 2a–e), is a lenticular, subvertical intrusive ore body, oriented N–S. With an approximate length of 85 m, a maximum width of 25 m and tens of meters high, Dongue Sul is the smallest of the four studied deposits (Figure 2a–c). In detail, this body presents a concentric zonation (Figure 2a,b). From the central part outwards, three units can be distinguished: Anelsonite core (magnetite–apatite rocks), surrounded by a breccia (oxide blocks cemented by secondary phosphates) and a massive Fe–Ti(–V) oxide envelope (Figure 2a). All of them are crosscut by a set of millimetric to decimetric veins filled by fine-grained secondary phosphates, with a slight dipping into the body (Figure 2b). The elliptic nelsonite core, approximately 12 m × 30 m across,

represents the highest relief in Dongue Sul (Figure 2c). It consists of millimetric crystals of Fe–Ti oxides and fluorapatite. Fluorapatite is often altered to (or pseudomorphosed by) secondary phosphates with a boxwork texture, similar to those filling the veins that cut the ore body. The intermediate breccia unit is 1 to 3 m thick and located between the nelsonite core and the massive oxides envelope, consisting of centimetric to decimetric, angular, massive Fe–Ti oxide blocks cemented by a whitish and highly porous matrix of secondary phosphates (Figure 2d). The secondary phosphates may be originated by alteration of primary fluorapatite by supergene, infiltrated fluids along the contact between the nelsonite core and the massive oxides. The Fe–Ti oxide massive, black envelope is more than 10 m thick, and surrounds the nelsonite core and the breccia (Figure 2e). Blocks detached from the walls accumulate at the base of the outcrop (Figure 2c). These massive oxides represent more than 50 modal % of Dongue Sul body (Figure 2a).

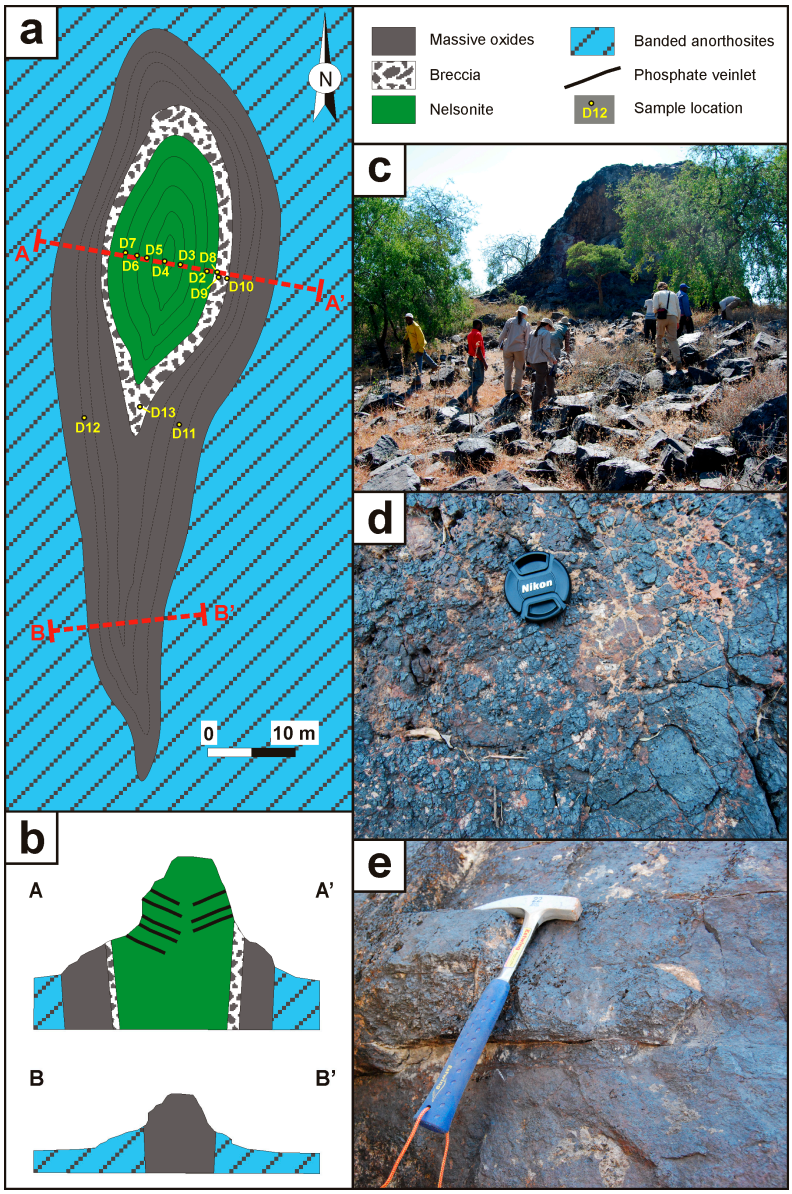

Figure 2. *Cont.*

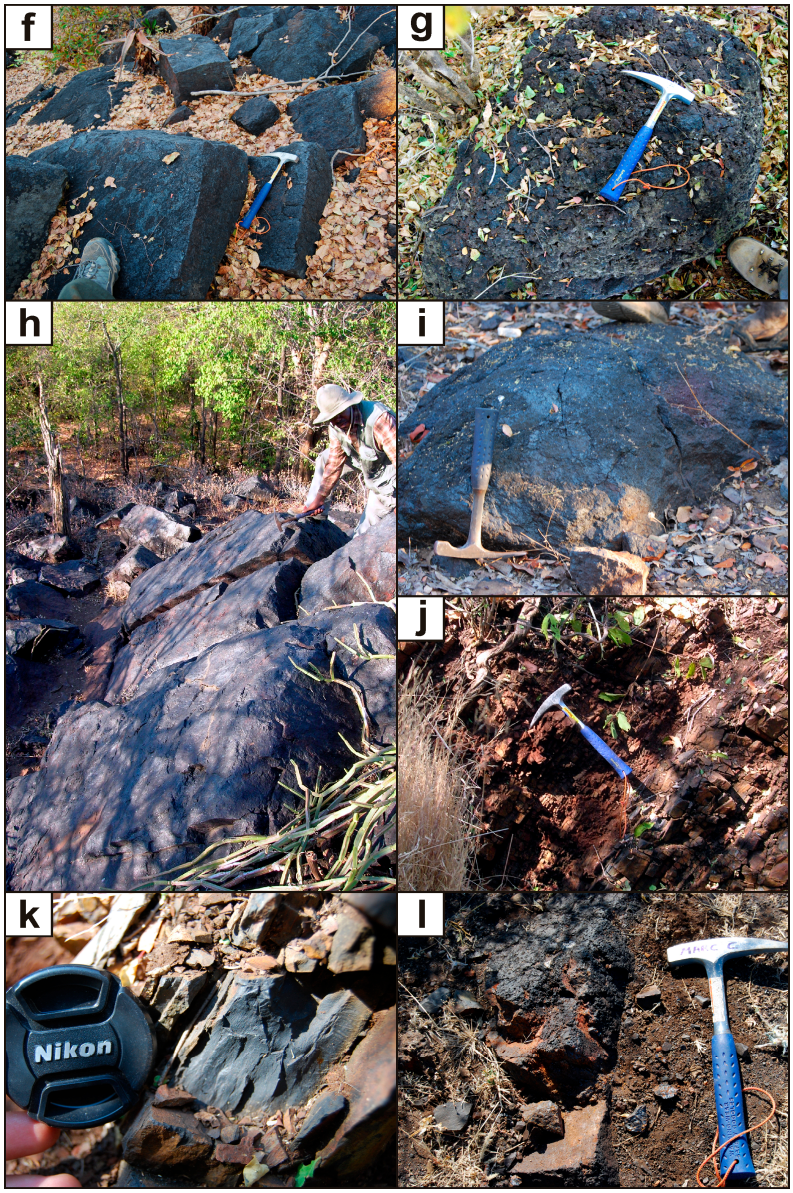

Figure 2. Mode of occurrence of the studied Fe–Ti(–V) oxide deposits of the Kunene anorthosite complex. Schematic geological map of the concentric, lenticular body of Dongue Sul (**a**); including two E–W cross sections (**b**); general view of the Dongue Sul ore body (**c**); massive Fe–Ti(–V) oxides (**d**) and Fe–Ti(–V) oxide breccia (**e**) outcrops in Dongue Sul; field images of the Fe–Ti(–V) oxide bodies of Tchimbueio, Tchingunguanganda and Chiange Velho: General view (**f**) and massive Fe–Ti(–V) oxide outcrop (**g**) in Tchimbueio; general view (**h**) and massive Fe–Ti(–V) oxide outcrop (**i**) in Tchingunguanganda; general view (**j**) and detail (**k**) of the banded Fe–Ti(–V) oxide outcrops, and massive Fe–Ti(–V) oxide outcrop (**l**) in Chiange Velho.

2.1.2. Tchimbueio

Tchimbueio consists of a set of isolated subvertical dikes, of 070 N approximate direction, with hectometric lengths, decametric widths and metric reliefs (Figure 2f). The dikes consist mainly of massive Fe–Ti oxides (Figure 2g), accompanied by minor oxide breccias and nelsonites. Fluorapatite crystals in Tchimbueio are less abundant and smaller (submillimetric) than in Dongue Sul. In Tchimbueio, breccias are related to a NE–SW fault, and are formed by Fe–Ti oxide fragments and a secondary Fe-oxyhydroxide matrix.

2.1.3. Tchingunguanganda

Tchingunguanganda occurs as a subvertical dike-like body, with a hectometric length and metric width and height. It crops out discontinuously at least along 500 m. It is approximately parallel to Tchimbueio, and consists exclusively of massive Fe–Ti oxides, which are poorly layered (Figure 2h,i).

2.1.4. Chiange Velho

Chiange Velho is the largest of the four studied deposits. It consists of two subvertical parallel dikes, with one end cropping out in the town of Chiange and extending up to 10 km [17] with an approximate direction of 150 N, describing a well-defined alignment in the satellite images [8]. The thickness of the body achieves its maximum (up to one hundred meters) at the vicinity of Chiange and decreases to about ten meters to the south (Figure 1). The southwestern dike, which is slightly longer, shows a millimetric, subvertical layering and is very fine-grained, to the point that Fe–Ti-oxide crystals are indistinguishable to the naked eye (Figure 2j–k). In contrast, the northeastern dike is massive and coarse-grained (Figure 2l). In the Chiange Velho outcrop, nelsonite also occurs as small bodies, but fluorapatite crystals are fewer and finer-grained than in all the above deposits.

3. Materials and Methods

3.1. Sampling

For the present study, 65 samples were selected from four different massive Fe–Ti(–V) oxide bodies located in the Angolan part of the KIC: Dongue Sul (20 samples), Tchimbueio (17 samples), Tchingunguanganda (6 samples), and Chiange Velho (22 samples).

3.2. Bulk Rock Geochemistry

Major, minor and trace elements of 33 selected samples were determined at ACME Analytical Laboratories Ltd. (Vancouver, BC, Canada) by purchasing the analytical packages 4A–4B (ICP-MS analysis after lithium metaborate-tetraborate fusion) and 1DX (ICP-MS analysis after hot modified Aqua Regia digestion.

3.3. Powder X-ray Diffraction (PXRD)

The samples were carefully ground using an agate mortar and pestle. Thirty-five samples were prepared by manual pressing of the powders, by means of a glass plate to get a flat surface, in cylindrical standard sample holders of 16 mm of diameter and 2.5 mm of height. The experimental profiles were obtained using a PANalytical X'Pert PRO MPD Alpha1 powder diffractometer (Scientific and Technological Centers of the Universitat de Barcelona or CCiT-UB, Barcelona, Spain) in Bragg-Brentano $\theta/2\theta$ geometry of 240 mm of radius, nickel filtered Cu Kα radiation (λ = 1.5418 Å), and 45 kV–40 mA. During analysis, sample was spun at 2 revolutions per second. Axial divergence Soller slits of 0.04 radians were used. Samples were scanned from 4° to 80° 2θ with step size of 0.017° and measuring time of 50 s per step, using a X'Celerator detector (active length = 2.122°), and a primary Ge monochromator. The detailed structural characterization and the mineral proportions were performed by full profile analyses of powder diffractograms using the software TOPAS version 4.0 (Rietveld method). This method was complemented with the mineral proportions obtained by examining the polished sections and polished thin sections.

3.4. Scanning Electron Microscopy (SEM)

The samples were prepared as polished sections and polished thin sections for their study under the optical microscope using reflected and transmitted light. A selection of these samples was examined on a Leica Cambridge S-360 scanning electron microscope (SEM) (CCiT-UB, Barcelona,

Spain), equipped with an energy-dispersive spectrometer (EDS). Operating conditions were 15 keV accelerating voltage and 5 nA in backscattered electron (BSE) mode.

3.5. Electron Microprobe Analyses (EMP)

Electron microprobe analyses were carried out using a CAMECA SX-50 electron microprobe (CCiT-UB, Barcelona, Spain). This instrument is equiped with four wavelength-dispersive spectrometers (WDS) and one energy-dispersive spectrometer (EDS). WDS analyses were conducted using a 20 keV acceleration voltage and 15 nA beam current. Standards used for calibration were hematite (Fe), rutile (Ti), periclase (Mg), rhodonite (Mn), corundum (Al), Cr_2O_3 (Cr), metallic vanadium (V), diopside (Si), sphalerite (Zn), NiO (Ni), wollastonite (Ca) and metallic Nb (Nb). The correction procedure PAP [47] was used to convert specimen intensity ratios into concentrations. The Ti Kβ overlap on the V Kα peak was corrected by the microprobe software.

The structural formulae calculations of titaniferous magnetite and ilmenite were performed on the basis of 4 and 3 oxygens, respectively, and using the criteria of [48] for the Fe^{3+} estimation. The composition of Fe–Ti(–V) oxides was plotted in triangular diagrams using the CSpace software [49]. Mineral and end member abbreviations are after [50].

High-resolution X-ray maps were obtained using a JEOL JXA-8230F field-emission electron microprobe at the Earth Observatory of Singapore (EOS). Operating conditions were 10 kV accelerating voltage, 50 nA beam current, 100 ms dwell time, 256 $\times$ 256 pixels in size.

Geothermometry

In order to calculate the temperature and oxygen fugacity of crystallization of Fe–Ti oxide magmas, the phases involved in the calculations (titaniferous magnetite and ilmenite) must be in equilibrium. However, titaniferous magnetite displays pervasive and varied exsolution phenomena. Therefore the bulk composition of the titaniferous magnetite prior to the exsolution has to be estimated. In addition, some subsolvus features include the presence of too-small-to analyze aluminous spinel lamellae [51]. For this reason, three methods to estimate the bulk magnetite composition were tested on two nelsonite samples from Dongue Sul: (a) Conventional point analysis coupled with BSE image analysis; (b) defocused beam; and (c) semiquantitative mapping.

Conventional point analysis involves performing a representative number of 1 µm-beam sized analyses of each phase in the exsolution (magnetite, ulvöspinel and aluminous spinel), in a 10 µm-sized, square area depicted in a SEM-BSE (backscattered electron) image. The area corresponding to each phase in the image was calculated using the ImageJ software. These areas, multiplied to the corresponding point analyses of each phase, gave an estimated bulk composition of titaniferous magnetite. The defocused beam method consists of analyzing exsolved titaniferous magnetite areas with a beam diameter of 20 µm, and the composition obtained was considered that of the pre-exsolved titaniferous magnetite. Finally, semiquantitative Fe, Ti, Al, Mg maps on square areas of 10 µm across were performed. The resulting images were processed with Image to obtain the average percentage of each element mapped.

Since the three methods gave similar outcomes, the defocused beam method was chosen because it was less time consuming. Representative massive Fe–Ti oxide samples of the four deposits (D-12, CHU-5, TCB-1 and CH-6) have been chosen for this part of the study, as well as nelsonites of Dongue Sul (D-2, D-3, D-6) Tchimbueio (TCB-15) and Chiange Velho (CH-20), and a layered rock of this later locality (CH-16).

4. Results

4.1. Bulk Rock Geochemistry

The four Fe–Ti oxide bodies of the KIC yield homogeneous TiO_2 contents (14.87–25.52 wt % TiO_2) and Fe/Ti ratios, with only two exceptions from the massive Tchimbueio ore body (Figure 3a;

Table S1, Supplementary Materials). TiO_2 values are higher than those from Damiao and Panzhihua, China ([3,52,53], respectively), Hestnes, Norway [54]; and similar to those reported in Tellnes, Norway ([11]; Figure 3b). Fe/Ti ratios are lower than those of Damiao (Figure 3a).

The KIC ore bodies contain very low SiO_2 (mostly below 3.61 wt % SiO_2, except two values around 20 wt % SiO_2 in Tchimbueio), when compared to other Fe–Ti(–V) oxide ore from other localities, since silicate phases are scarce (Figure 3b; Table S1). V contents range from 1520 to 2730 ppm (2300 ppm V on average), and are within those of Norwegian deposits ([54]; Figure 3c). Remarkable CaO and P_2O_5 contents are detected in the nelsonites, pointing to the concentration of fluorapatite in these rocks (Figure 3d,e; Table S1). It is worth noting that breccias contain high P_2O_5 but low CaO. Therefore phosphates other than fluorapatite might be responsible of the P_2O_5 content in such breccias (Figure 3d). The nelsonites from the KIC draw a CaO-P_2O_5 correlation similar to that observed in Damiao (China), Kydlandsvatn and Hestnes (Norway) and Grader (Canada; Figure 3d). In contrast, the P_2O_5-TiO_2 versus P_2O_5 correlation is steeper than that drawn by the data of Damiao or Hestnes (Figure 3e).

Rare earth elements (REE) are enriched in studied nelsonites, whereas their concentrations are lower in breccias, layered and massive bodies (Figures 3f and 4; Table S1). This observation suggests that the REE-enrichment is controlled by the occurrence of apatite. REE patterns show slight enrichment of light (LREE: La, Ce, Pr, Nd) relative to medium (MREE: Sm, Eu, Gd) and heavy (HREE: Tb, Dy, Ho, Er, Tm, Yb, Lu, Y) REE when normalized to chondritic values, depicting negative slopes (Figure 4). This relative enrichment in LREE is also observed in other Fe–Ti(–V) oxide ores from other localities [3,52–55]. Studied nelsonites show subdued negative to nil Eu anomalies. Tenuous positive anomalies of Ce occur in some samples from Tchimbueio (Figure 4). The concentration of REE is similar to that of Kydlandsvatn and Damiao deposits and overall, lower than those of Hestnes deposit (Figure 3f).

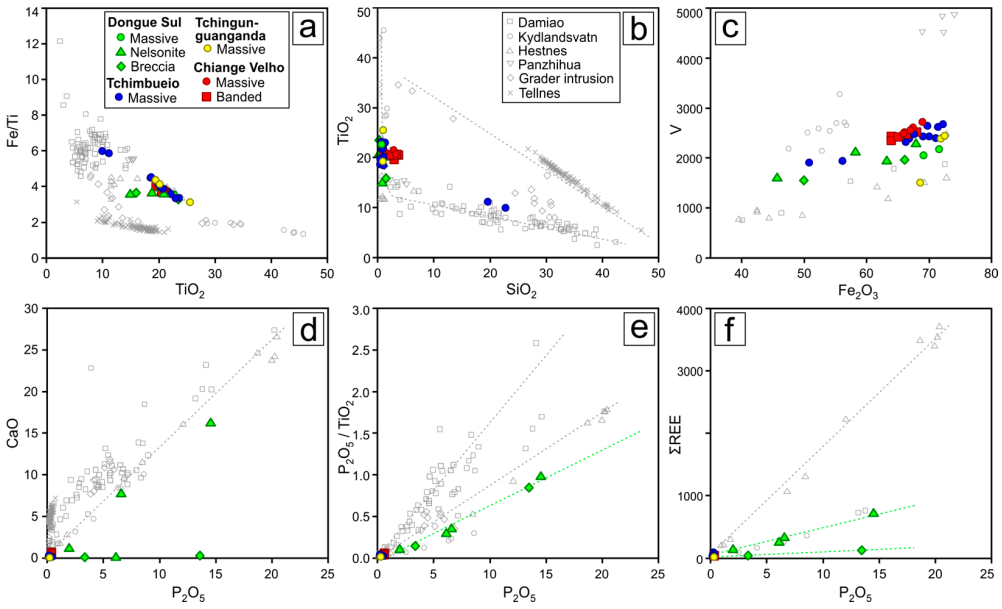

Figure 3. Binary major and trace element variation diagrams of whole-rock oxide ore from the Kunene Anorthosite Complex: (**a**) Fe/Ti vs. TiO_2, (**b**) TiO_2 vs. SiO_2, (**c**) V vs. Fe_2O_3, (**d**) CaO vs. P_2O_5, (**e**) P_2O_5/TiO_2 vs. P_2O_5, (**f**) ∑REE vs. P_2O_5. Published data from other localities are shown for comparison Damiao: [3,52]; Kydlandsvatn and Hestnes: [54]; Panzhihua: [53]; Grader intrusion: [56]; Tellnes: [11]. (**a**) is based on [6]; and (**b**) is based on [3]. TiO_2, SiO_2, Fe_2O_3, CaO, P_2O_5 are in wt %, V and ∑REE (La–Lu and Y) are in ppm.

4.2. Mineralogy and Textures

The studied ore bodies are characterized by a simple mineral composition, which develops complex textures. In order of abundance, ore bodies are formed by: Titaniferous magnetite, ilmenite, spinel and fluorapatite, and minor olivine, phlogopite, graphite, as well as supergene Fe-oxyhydroxides, Al hydroxides and phosphates (Figures 5 and 6a–r).

All the studied samples can be classified into two groups, according to the microtextures of the main mineralogy. The first group corresponds to the samples from Dongue Sul, Tchingunguanganda and Tchimbueio. This group is dominated by titaniferous magnetite (from 62 to 80 wt %), and ilmenite as the second most abundant phase (4–23 wt %). Aluminous spinel is less abundant but systematically present (2–7 wt %). Other minor phases include fluorapatite, goethite, hematite, and graphite (below 10 wt %; Figure 5). The second group corresponds to the samples from Chiange Velho. Titaniferous magnetite is also the most abundant mineral (44–49 modal %), but ilmenite has similar proportions (32–38 modal %). The cell parameters of ilmenite are smaller, suggesting a major geikielite component in the solid solution [57]. Aluminous spinel is also present (5–11 modal %), and graphite is only observed in one sample. The mineralogy and abundance of secondary minerals are similar in both groups (usually less than 1 modal %).

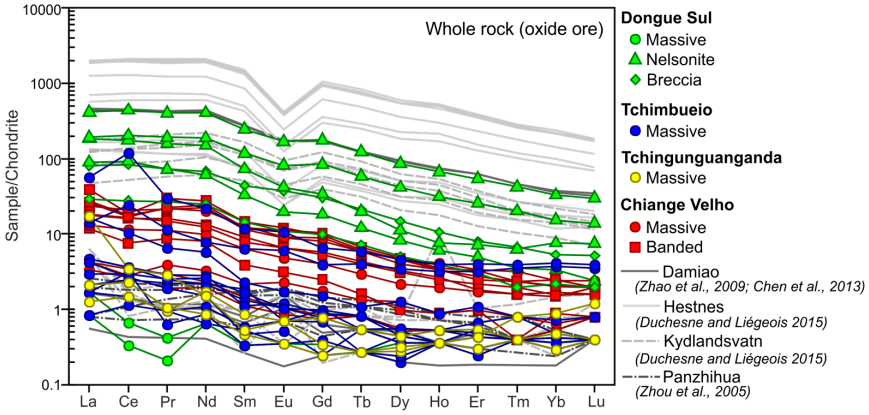

Figure 4. Spider diagram depicting the chondrite-normalized REE composition of massive oxide, breccia and nelsonite ores of the four occurrences studied in the KIC (chondrite values are after [58]).

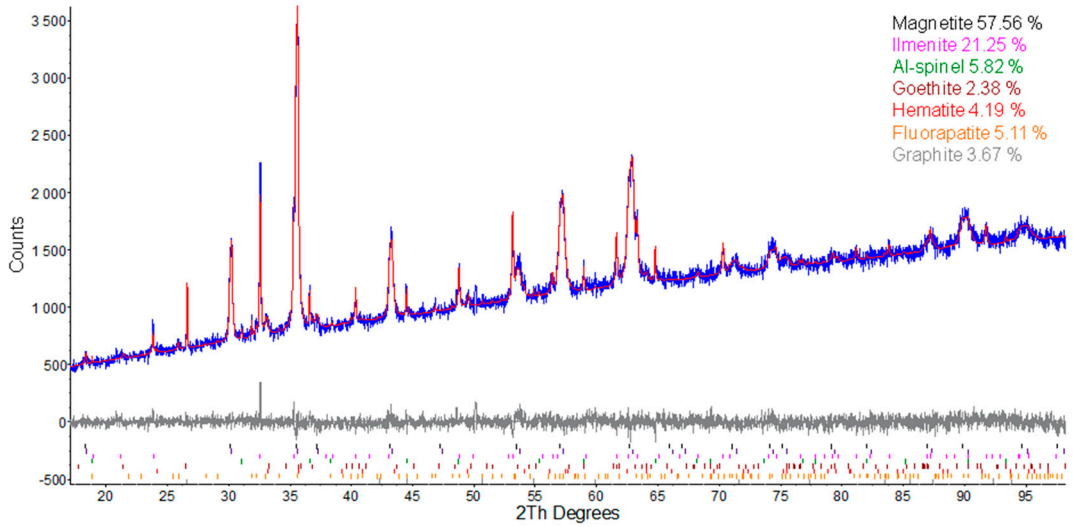

Figure 5. X-ray diffractogram (blue) with the quantitative mineralogy of sample D-4 from Dongue Sul, including the sum of the individual reference diffractograms and the background (red), and the residue (grey).

In general, in Dongue Sul, Tchingunguanganda and Tchimbueio, mineral textures denote equilibrium (Figure 6a,b), despite some crystals may present irregular or even jagged boundaries (Figure 6j). In contrast, in Chiange Velho, minerals define a micrometric layering (Figure 6h,i,n) and show evidences of recrystallization under shearing (mylonitic fabric). Finally, in all ore bodies, titaniferous magnetite shows subsolvus textures (Figure 6b–g).

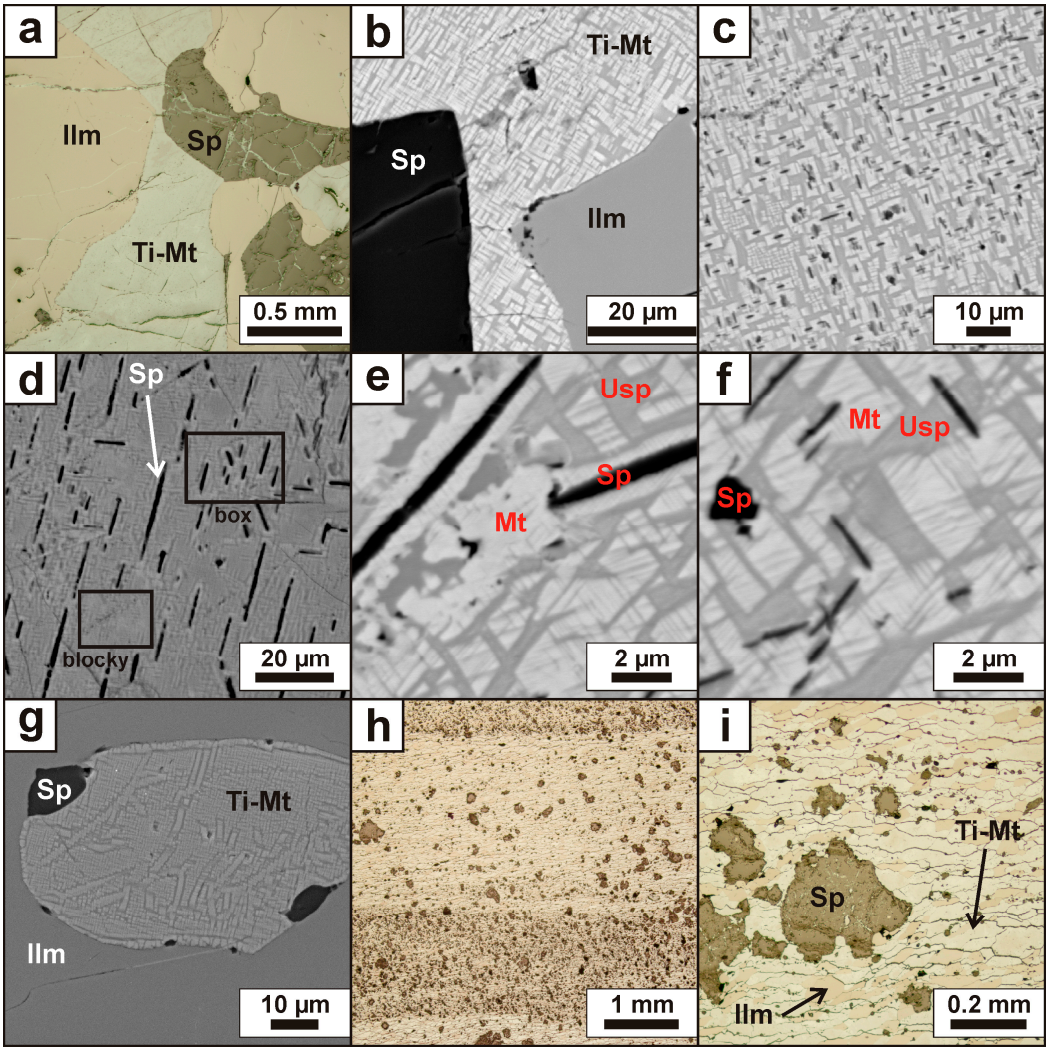

Figure 6. *Cont.*

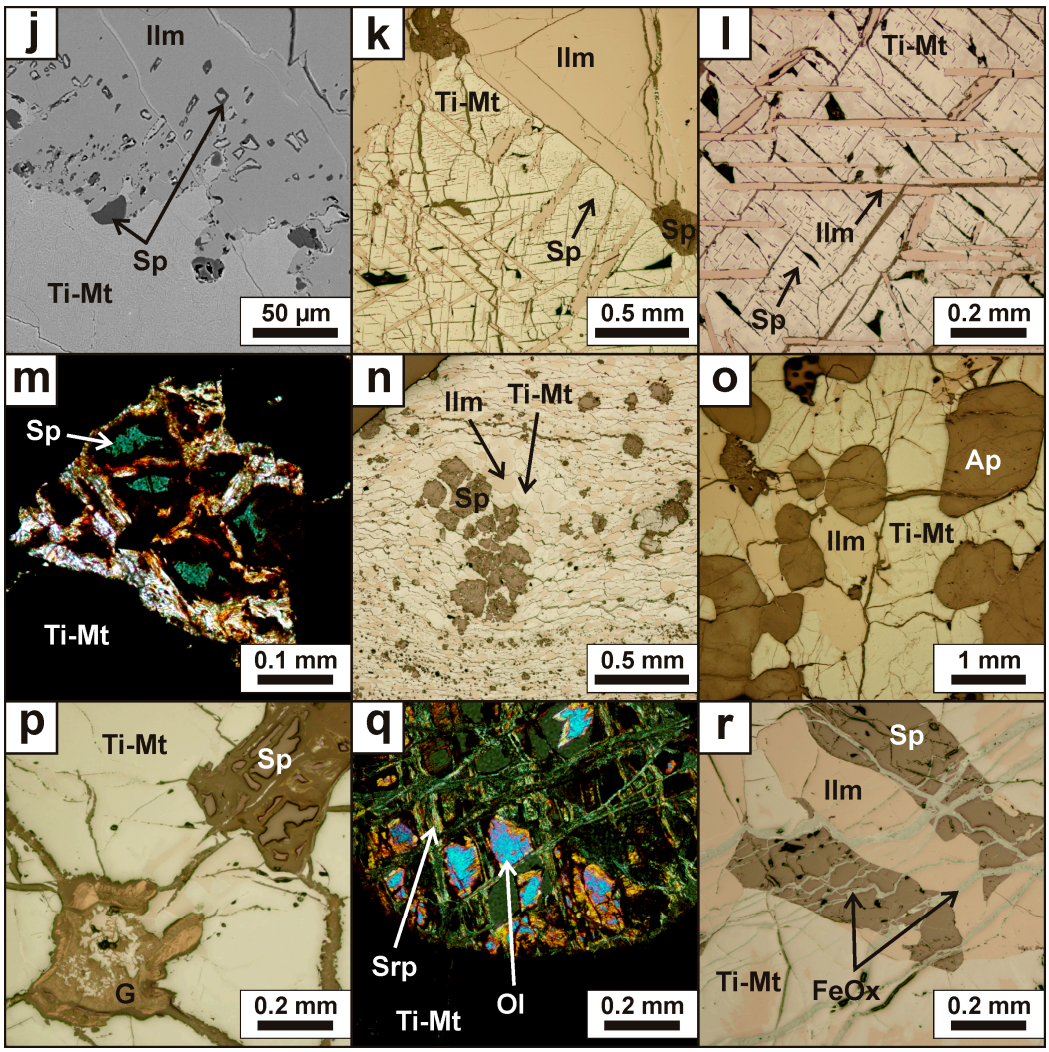

Figure 6. Optical (a,h,i,k,l,n,o,p,r reflected light; m, transmitted plane parallel light; and q, transmitted light with crossed polars) and backscattered electron (BSE) micrographs (b,c,d,g,j: CCiT-UB; e,f: EOS) of the most representative textures in the massive magnetitites, layered magnetitites and nelsonites from Dongue Sul, Tchimbueio, Tchingunguanganda and Chiange Velho, Kunene Complex (SW Angola): (**a,b**) equilibrium textures between titaniferous magnetite (Ti-Mt), ilmenite (Ilm) and spinel (Sp) in samples D-12b (**a**) and TCB-1a (**b**); the SEM-BSE image depicts blocky exsolution features in titaniferous magnetite (**b**); (**c**) blocky exsolution in titaniferous magnetite (sample TCB-1a); (**d**) blocky and box exsolutions in titaniferous magnetite (sample CHU-5); (**e,f**) close-up of exsolutions in titaniferous magnetite: magnetite (Mt) lamellae in a matrix of ulvöspinel (Usp), surrounding spinel lamellae (sample D-3a); (**g**) aluminous spinel and exsolved titaniferous magnetite inclusions in ilmenite (sample D-12a); (**h,i**) elongated titaniferous magnetite and ilmenite in a banded array (sample CH-16); (**j**) irregular boundary between titaniferous magnetite and ilmenite, the latter with pervasive inclusions of aluminous spinel and titaniferous magnetite (sample D-12a); (**k,l**) elongated ilmenite crystals oriented according to {111} magnetite planes (sample CH-20); (**m**) fractured, angular aluminous spinel crystal in titaniferous magnetite (sample CH-15b); (**n**) aluminous spinel porphyroclasts rotated by shear stress in a titaniferous magnetite–ilmenite mylonitic massive ore groundmass (sample CH-16); (**o**) equilibrium texture between fluorapatite, ilmenite and titaniferous magnetite (sample D-2); (**p**) nematomorphic aggregate of graphite in titaniferous magnetite (sample CHU-1); (**q**) olivine crystal altered to serpentine, in titaniferous magnetite (sample CH-15b); (**r**) Fe-oxyhydroxide (FeOx) veinlets crosscutting titaniferous magnetite, ilmenite and aluminous spinel (sample TCB-1a).

4.2.1. Titaniferous Magnetite

Titaniferous magnetite is the most abundant mineral in all ore bodies that were studied, ranging from 40 modal % to 80 modal % in massive magnetitites, and from 40 modal % to 50 modal % in nelsonites.

Firstly, in the Dongue Sul, Tchingunguanganda and Tchimbueio ore bodies, titaniferous magnetite develops millimetric to centimetric, anhedral, non-homogeneous crystals (Figure 6a,b). They show three kinds of exsolutions; almost one of them is always present, and two or more can coexist in the same sample. The first type consists of magnetite lamellae aggregates or micrometric rectangular prisms surrounded by ulvöspinel (Figure 6b–d), which is referred to as blocky-type [59] or cloth-textured [60] in the literature; it may include tiny spinel lamellae (Figure 6c). The second type consists of spinel lamellae, with variable lengths (microns to tens of microns) and widths of less than a micron. Spinel lamellae are oriented along the {100} planes of the host mineral, and are wrapped by a magnetite micrometric envelope that separates the lamellae from the surrounding ulvöspinel (Figure 6d). Reference [23] defined this texture as box-type. Box-type lamellae have been also observed in Bjerkrem-Sokndal, Norway [60], in the Upper Zone of the Bushveld Complex, South Africa [61] and in the Kovdor phoscorite–carbonatite complex, Russia [62]. In some cases, higher magnification images reveal signs of two generations of exsolutions (Figure 6e,f). It must be noted that ulvöspinel was not identified by XRD, and it has been probably subsolidus oxidated to ilmenite [63].

Finally, titaniferous magnetite also contains exsolved lamellae of ilmenite, or less frequently, irregular-shaped, which are described in the following subsection. Titaniferous magnetite grains containing ilmenite exsolution lamellae may also contain magnetite–ulvöspinel exsolutions, but the latter are less developed.

In addition, titaniferous magnetite develops submillimetric inclusions in ilmenite, frequently associated to tiny subhedral spinel crystals. In this case, titaniferous magnetite may also present blocky-type exsolutions (Figure 6g).

In contrast, in banded rocks from Chiange Velho, titaniferous magnetite crystals are subhedral, smaller (about one hundred microns in length), elongated (Figure 6h,i) and may present finer and irregular-shaped magnetite–ulvöspinel exsolutions.

4.2.2. Ilmenite

Ilmenite is the second most abundant mineral in massive magnetitites (from 10 modal % to 30 modal %) and the third in nelsonites (from 5 modal % to 20 modal %). In the layered magnetitites from Chiange Velho, the ilmenite content may reach 40 modal %.

On one hand, in Dongue Sul, Tchingunguanganda and Tchimbueio, ilmenite forms three different types of textures. Firstly, it forms millimetric euhedral to subhedral and homogeneous crystals (Figure 6a). They often develop straight boundaries, but can also show irregular and jagged boundaries (Figure 6j). This is the most common type of ilmenite in the four deposits studied. On the other hand, in layered magnetitites from Chiange Velho, ilmenite occurs as subhedral elongated crystals, up to one hundred microns long (Figure 6k,l). Furthermore, in some massive magnetitites from Chiange Velho, ilmenite develops Trellis exsolutions in titaniferous magnetites. These consist of lamellae with lengths of hundreds of microns and widths of tens of microns, following {111} magnetite planes [59] (Figure 6k,l).

4.2.3. Aluminous Spinel

The content of spinel in the four ore bodies is up to 11 modal %, with no remarkable differences among rock types or ore bodies. Aluminous spinel can be classified into two textural groups. First, it develops millimetric to submillimetric and euhedral to subhedral crystals, with straight boundaries (Figure 6a,b,m), sometimes included in titaniferous magnetite (Figure 6g) or ilmenite (Figure 6j). It may present fractures filled with Al hydroxides and Fe-oxyhydroxides (mainly hematite) (Figure 6m).

It must be noted that this group of spinels are strongly fractured and deformed (eventually rotated) in the sheared lenses from Chiange Velho (Figure 6n). Secondly, it occurs as exsolution lamellae in titaniferous magnetite (Figure 6c–f).

4.2.4. Accessory Minerals

Fluorapatite is mainly found in nelsonites from Dongue Sul and Tchimbueio, and in some layered rocks from Chiange Velho, and its abundance and size varies from site to site. Crystals in Dongue Sul are millimetric and represent almost 50 modal % of the rock, whereas in Chiange Velho they are micrometric and are much less abundant (up to 2%). Apatite develops euhedral crystals with rounded boundaries (Figure 6o) and always presents abundant vitreous and bifasic fluid inclusions. Frequently, apatite crystals are altered to secondary phosphates, which have been formed as a result of weathering. An X-ray diffraction analysis of a nelsonite from Dongue Sul allowed the identification of wavellite, and the presence of other secondary phosphates cannot be discarded.

Graphite develops spherulitic or nematomorphic aggregates, and is very common in fractures (Figure 6p). It is present in all kinds of rocks of the four deposits, except in the layered rocks from Chiange Velho (where only one sample contains graphite). It frequently represents less than 1 modal % of the rock.

Olivine and phlogopite are very scarce, as they were only observed in one nelsonite sample from Chiange Velho, representing less than 5 modal % and 2 modal %, respectively. Olivine crystals are millimetric and euhedral to subhedral, and have an average composition of Fo_{74}. They are strongly altered to serpentine group minerals (Figure 6q). Phlogopite forms subhedral crystals in tabular aggregates.

Other minerals are secondary Fe-oxyhydroxides, such as hematite and goethite, and an Al hydroxide (possibly gibbsite or böhmite). These minerals are located in late veins, in boundaries between crystals and as replacements (Figure 6r).

4.3. Mineral Chemistry

4.3.1. Titaniferous Magnetite

Titaniferous magnetite from the four oxide bodies display a wide range of Ti contents (Figure 6a), irrespectively of the rock or textural types described above (Figure 6b). Titaniferous magnetite contains between 2.27 and 32.47 wt % TiO_2, equivalent to $Usp_{7–90}$, and up to 0.85 wt % V_2O_3 (0.27 wt % V_2O_3 on average; Figure 6a; Table S2). Zn content is low (below 1.53 wt % ZnO) when compared to the typical significant gahnite component of this kind of ore bodies [54] (Table S2). Titaniferous magnetite in Dongue Sul and Tchimbueio yield a wider range of compositions between the magnetite and ulvöspinel end members, and have higher ulvöspinel component than those of Tchingunguanganda and Chiange Velho. Massive rocks from Chiange Velho show a slightly lower Ti content in titaniferous magnetite (Figure 7a).

Finally, the qualitative element maps obtained in areas with blocky- and box-type exsolutions allow identifying the different phases in the different subsolvus phenomena observed (Figure 8). Blocky type exsolutions are constituted by a magnetite core (with no Ti and higher Fe), surrounded by an ulvöspinel envelope (high Ti and lower Fe; Figure 8). Box-type exsolutions are formed by aluminous spinel lenses or lamellae (black in the BSE image, with high Mg and Al, and no Ti and Fe), surrounded by magnetite (light grey) and in turn, by ulvöspinel (dark grey, Figure 8). These observations are coincident with those of [23].

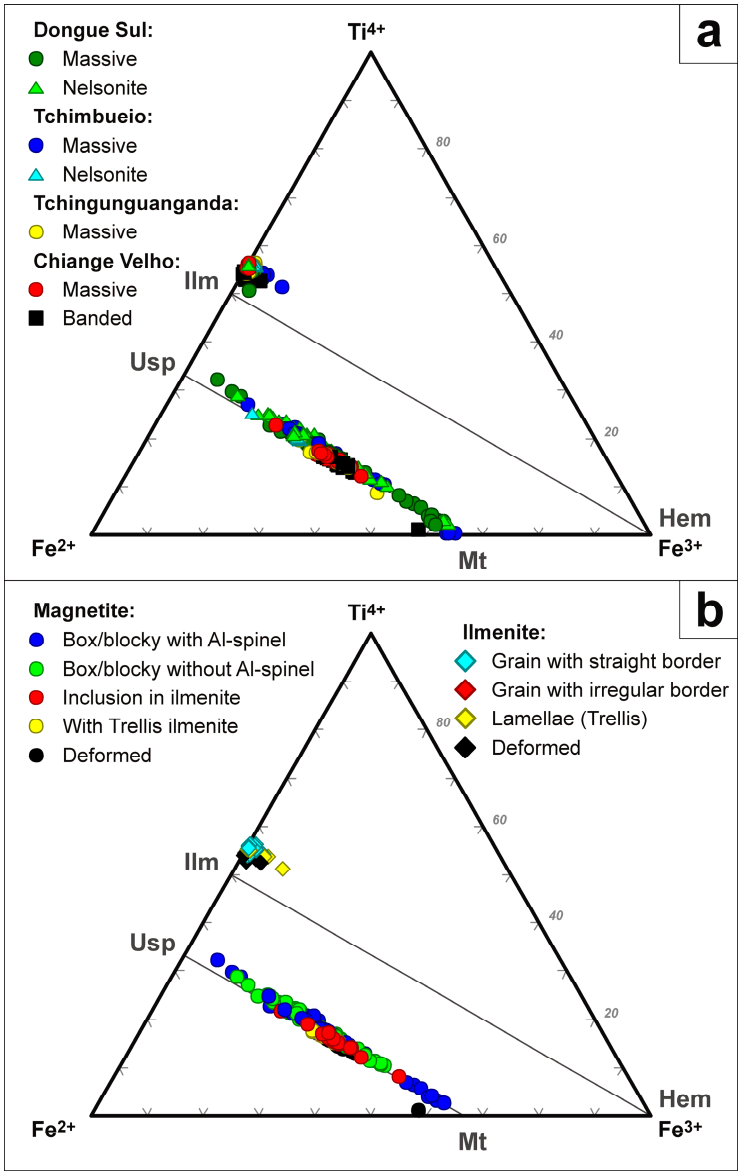

Figure 7. Fe^{2+}–Ti–Fe^{3+} triangular plots representing the composition of magnetite and ilmenite in the KIC according to the lithology (**a**); and the textural group (**b**). Legend: Ilm = ilmenite ($Fe^{2+}TiO_3$), Hem = hematite ($Fe^{3+}{}_2O_3$), Usp = ulvöspinel ($Fe^{2+}{}_2TiO_4$), Mt = magnetite ($Fe^{2+}Fe^{3+}{}_2O_4$). It must be noted that the plotted compositions are determined by the Fe^{2+}/Fe^{3+}calculation method used.

4.3.2. Ilmenite

In general, ilmenite from Dongue Sul, Tchimbueio, Tchingunguanganda and Chiange Velho have similar compositions, with 50.47–55.11 wt % TiO_2 (0.93–1.00 apfu Ti), low hematite component (Figures 7a and 9a), Mg ranging from 3.97 to 6.29 wt % MgO (Figure 9b) and Cr below 0.06 wt % Cr_2O_3 (Table S3). With regards to the textural groups described above, the deformed grains of layered rocks from Chiange Velho contain lower Ti (50.47–50.91 wt % TiO_2, 0.93–0.94 apfu Ti), higher hematite (up to 7.07 mol %) and lower geikielite components (14.09 mol % on average) than the grains with straight and irregular boundaries, and the Trellis exsolution ilmenites (52.46–55.11 wt % TiO_2, 0.97–1.00 apfu Ti, and up to 2.44 mol % Hem, 18.96 mol % Gk on average; Figure 9c; Table S3).

There are no major differences among the different textural types in terms of Fe, Mg and Mn contents (hematite, geikielite and pyrophanite components, respectively; Figure 9c,d).

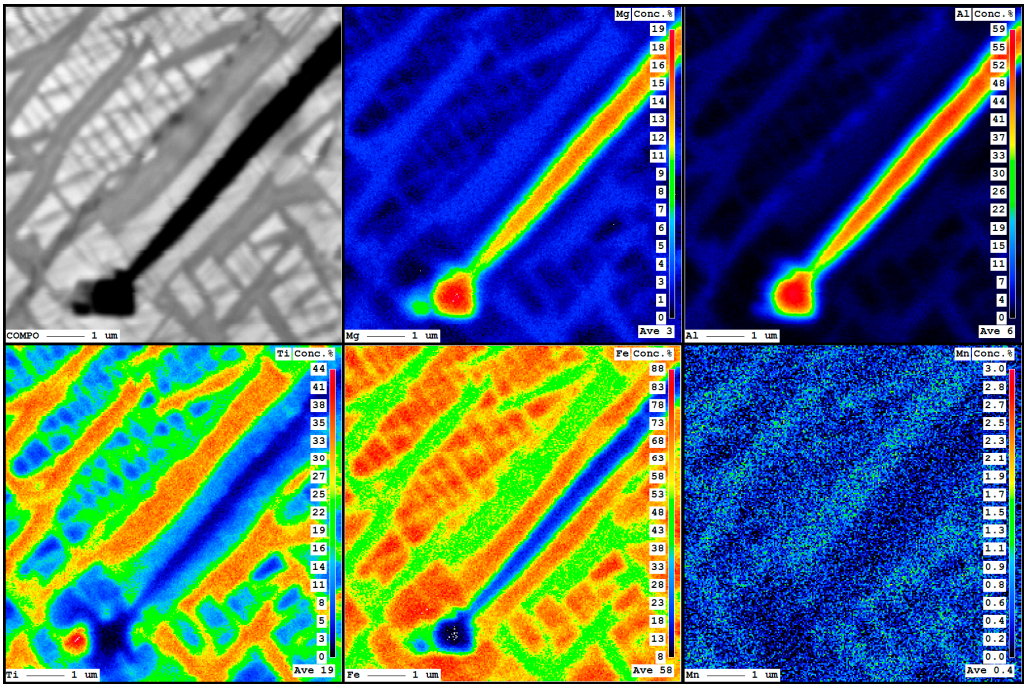

Figure 8. BSE image and Mg, Al, Ti, Fe and Mn X-ray maps showing aluminous spinel–magnetite–ulvöspinel exsolutions in titaniferous magnetite (EOS).

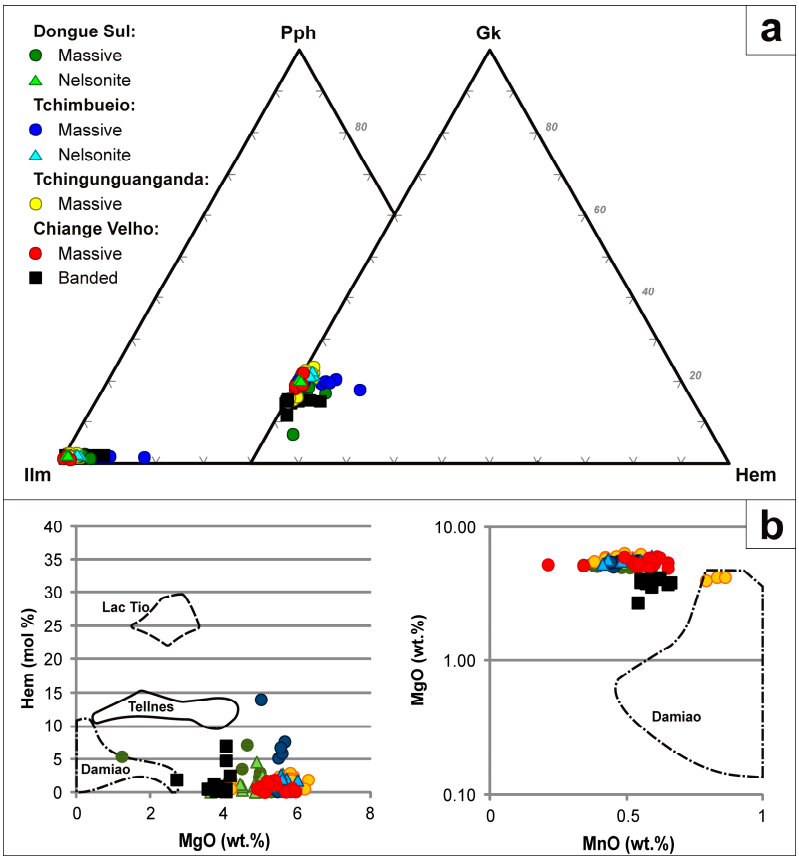

Figure 9. *Cont.*

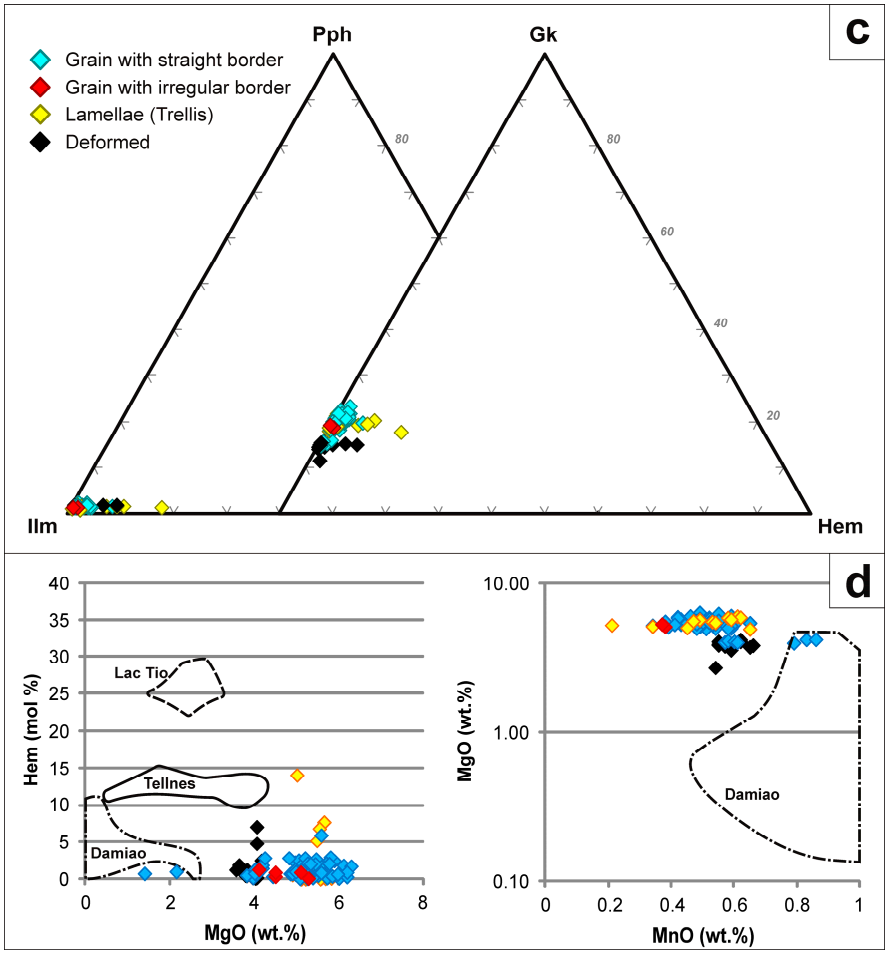

Figure 9. Composition of ilmenite from the KIC: (**a**,**c**) Ilmenite–pyrophanite–hematite (left) and ilmenite–geikielite–hematite (right) components of ilmenite; (**b**,**d**) hematite versus MgO (based on [6]) and MnO vs. MgO (based on [3]); according to the lithology (**a**,**b**) and the textural group (**c**,**d**). Legend: Ilm = ilmenite ($Fe^{2+}TiO_3$), Pph = pyrophanite ($MnTiO_3$), Hem = hematite ($Fe^{3+}{}_2O_3$), Gk = geikielite ($MgTiO_3$).

4.3.3. Aluminous Spinel

All the textural types are aluminous spinel with dominant Mg, Al and lower Fe^{2+} and Fe^{3+} (Figure 10; Table S4), with no important variations in composition between the different types of rocks (massive, nelsonite and banded) and localities. As titaniferous magnetite, aluminous spinel contains low Zn (below 1.13 wt % ZnO) (Table S4). Quantitative analyses were only performed in grains larger than 1 µm (millimetric, euhedral to subhedral crystals, and those associated to titaniferous magnetite included in ilmenite, excluding the aluminous spinel lenses in exsolutions). Nevertheless, qualitative element maps were obtained, of areas with a side length of 10 µm (Figure 8). The images confirm that exsolution lamellae concentrate Mg and Al, so they classify as aluminous spinel as well.

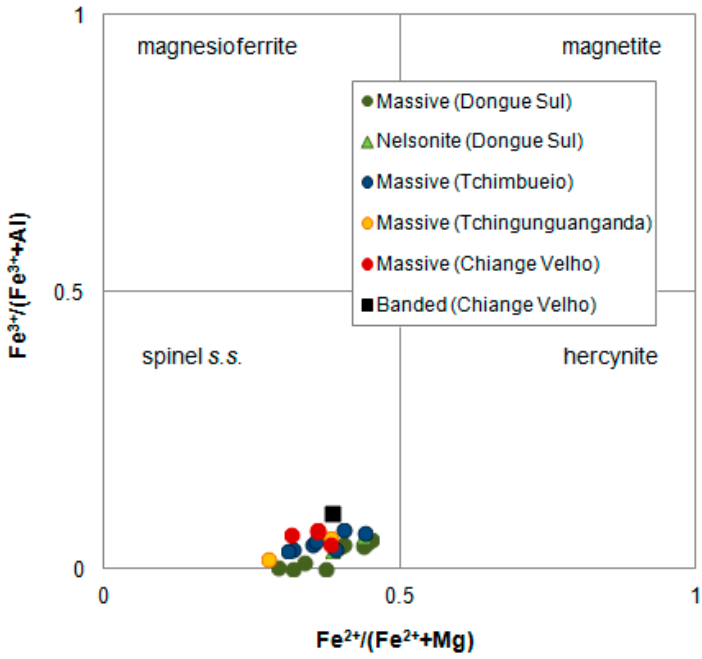

Figure 10. Binary diagram showing the composition of the aluminous spinel crystals analyzed.

4.4. Geothermobarometry

Temperature and oxygen fugacity were calculated by means of the ilmenite–magnetite thermo-oxybarometry worksheet built by [64] since it takes into account important concentrations in minor elements such as Al, Cr, Mg and Mn, typical of oxides occurring in intermediate to basic rocks. An approximate crystallization pressure was required to run the worksheet, and 8 kbar was chosen as it corresponds to the emplacement pressure of the anorthosites of the Kunene Complex estimated by [11]. However, it has been observed that temperature and oxygen fugacity do not significantly vary with pressure.

Firstly, the calculated temperature values range from 600 °C to 820 °C and the oxygen fugacity, from $10^{-14.7}$ to $10^{-24.7}$ (Figure 10). The T-fO_2 diagram shows that most results plot in the field delimited by the graphite–CO_2 (CCO) and the wüstite–magnetite (WM) buffers, and only a few plot below the WM and iron–wüstite (IM) curves. This is coherent with the presence of magnetite and graphite (Figure 6s), and the low hematite component in ilmenite (Figure 9), suggesting a reducing system.

Secondly, calculated values do not cluster according to rock type or ore body. In other words, results obtained in samples of the same lithology or occurrence yield a wide range of temperature and oxygen fugacity. In fact, different samples from the same nelsonite unit from Dongue Sul yield temperatures with a difference of 100 °C (Figure 11).

It must be remarked that the worksheet did not allow the calculation of the temperature and oxygen fugacity neither of layered rocks from Chiange Velho nor rocks with lamellar ilmenite exsolutions in titaniferous magnetite, probably because their final equilibrium temperatures are below the calculation range of the worksheet (~600 °C). Furthermore, the values obtained in the Angolan part of the KIC are similar to those calculated in the Namibian part by [11]: Between 690 and 730 °C, and from 10^{-15} to 10^{-17}, below the quartz–fayalite–magnetite (QFM) curve, by applying the thermo-oxybarometer by [65] in Fe–Ti oxides contained in anorthosites.

The temperature range is comparable to that delimited by nelsonites from other localities, such as the Duluth Complex, USA [66], different deposits in Québec, Canada [12,66] and Rogaland, Norway [63], calculated with the [67] thermo-oxybarometer. In contrast, the KIC values do not draw a path parallel to QFM curve and the oxygen fugacities are slightly lower than in the aforementioned deposits (Figure 11).

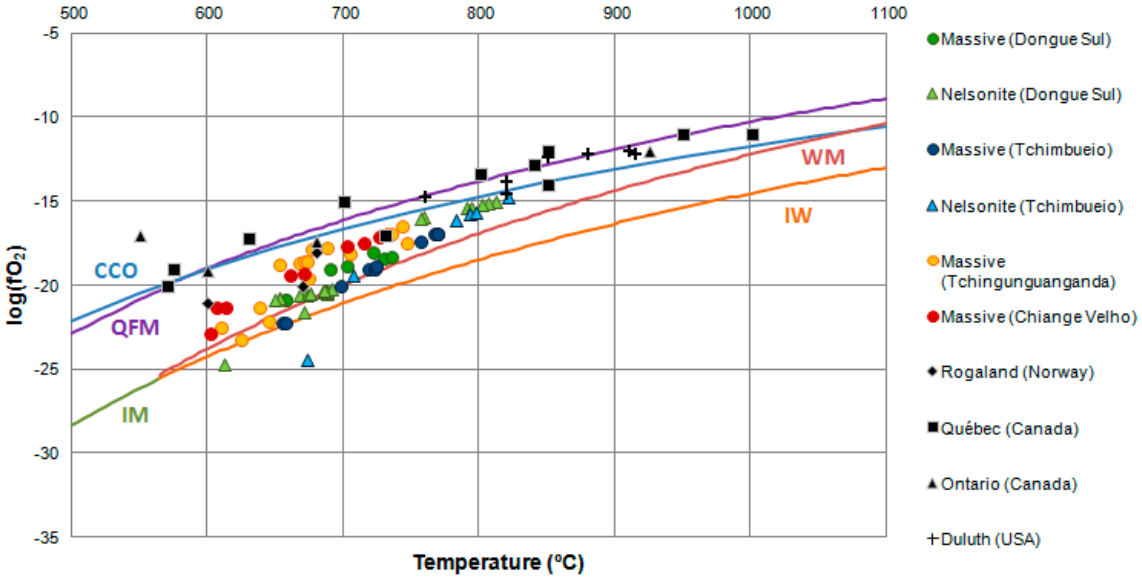

Figure 11. Thermo–oxybarometry plot obtained with the worksheet proposed by [64] using selected titaniferous magnetite defocused beam analyses and ilmenite point analyses. Data from Egersund (Rogaland, Norway) is from [63]; data from Duluth (USA), Degrosbois, St. Charles and Ellen Lake (Québec, Canada), and Pusey (Ontario, Canada) are from [66]; and data from Labrieville, Port Cartier and St. Charles (Québec, Canada) are from [12]. IW (iron–wüstite), WM (wüstite–magnetite), IM (iron–magnetite) and QFM (quartz–fayalite–magnetite) buffer curves are from [68], and CCO (graphite–CO_2) buffer curve is from [69].

5. Discussion

5.1. T-fO_2 Evolution of the Studied KIC Fe–Ti(–V) Oxide Bodies

The T-fO_2 values of the KIC are significantly lower compared to those of the Fe–Ti–P system from the literature. Firstly, according to [64], titaniferous magnetite–ilmenite solidus is around 1300 °C and [12] estimated that the presence of apatite lowers the melting temperature to 850–1000 °C in nelsonites. Furthermore, the data obtained do not follow a trend, defined by a concentration of values from massive oxide rocks at higher temperatures and fugacities (above 1300 °C and fO_2 = 10^{-11}–10^{-8}) than those from nelsonites (850–1000 °C and fO_2 = 10^{-15}–10^{-10} approximately; Figure 11). Secondly, the temperatures and fugacities plot in a continuous wide range, and are not grouped according to deposits or lithologies (Figure 11). On this basis, a straightforward explanation of the low T and fO_2 indicated by the thermo-oxybarometry is that a later re-equilibration could have occurred. This is supported by the presence of jagged boundaries between titaniferous magnetite and ilmenite (Figure 6m), which are a typical reaction rim as defined by [60,70], indicating that at least one of the oxide grains have re-equilibrated subsolvus at lower T. In addition, [10] obtained similar temperatures and oxygen fugacities in the Namibian KIC, which were interpreted as a product of later re-equilibration as well.

The KIC Fe–Ti oxides display a variety of subsolvus features, mainly in the system magnetite–ulvöspinel (–aluminous spinel) and locally titaniferous magnetite–ilmenite (Trellis exsolutions). The maximum exsolution temperature for the magnetite–ulvöspinel pair obtained experimentally by [71] is ~450 °C, from box-type exsolved titaniferous magnetites similar to the ones described in the present work. Thus, in all cases, the temperature resulting from thermo-oxybarometer calculations is higher than this solvus, so the re-equilibration between titaniferous magnetite and ilmenite should have occurred prior to exsolution. The aluminous spinel exsolution lamellae are interpreted as previous to the magnetite–ulvöspinel exsolution, as stated by [72,73] and demonstrated experimentally by several authors. Reference [74] obtained the magnetite–hercynite solvus at

860 ± 15 °C. In addition, reference [71] observed that magnetite and ulvöspinel homogenized to titaniferous magnetite when heating natural samples with box-type exsolutions to 500 °C, but spinel lamellae remained intact. Therefore, in the KIC, the aluminous spinel exsolution could act as the base where magnetite–ulvöspinel exsolutions would nucleate on (Figure 12).

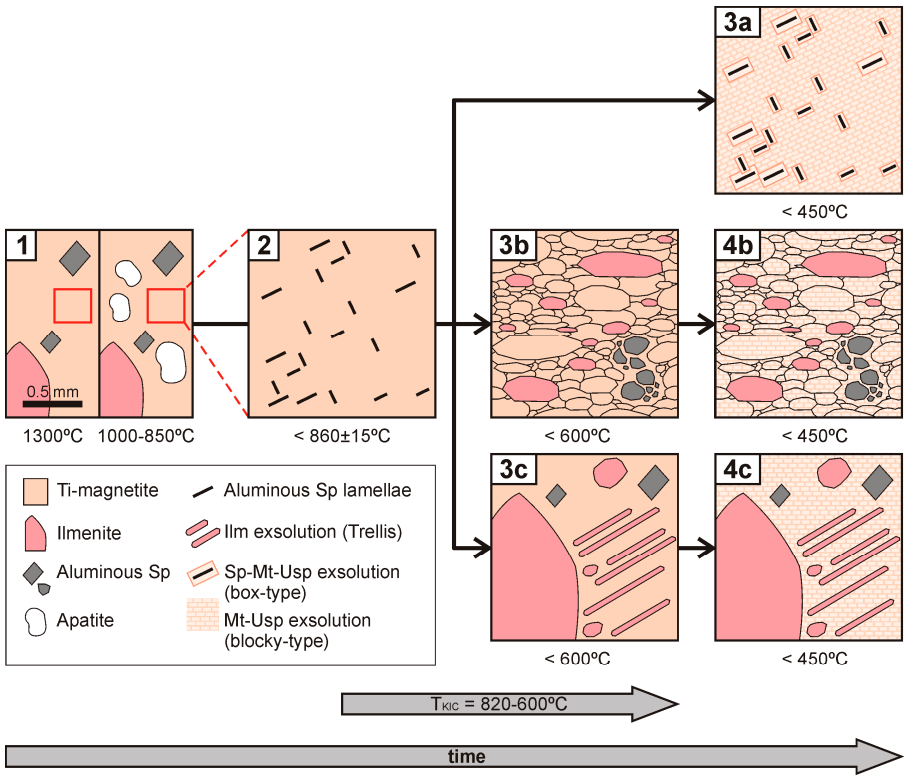

Figure 12. Simplified, schematic model representing the evolution of the different textural features observed in the studied KIC Fe–Ti(–V) oxide bodies: (**1**) Titaniferous magnetite, ilmenite and aluminous spinel formation in massive oxide rocks at 1300 °C (left) and nelsonites at 850–1000 °C (right); (**2**) exsolution of aluminous spinel in titaniferous magnetite; (**3b**) deformation causing the mylonitic fabric observed in Chiange Velho; (**3c**) formation of Trellis oxy-exsolutions in massive rocks from Chiange Velho; (**3a**,**4b**,**4c**) magnetite–ulvöspinel exsolution. Note that the temperature varies on the composition of the exsolved mineral, and that the magnetite–hercynite and magnetite–ulvöspinel solvus are bell-shaped. Therefore, 860 ± 15 °C and 450 °C is maximum temperatures of exsolution at $Usp_{50}Mt_{50}$ and $Her_{50}Mt_{50}$, respectively.

Finally, as previously discussed, the worksheet used did not allow obtaining the temperature and oxygen fugacities of the Fe–Ti oxide rocks from Chiange Velho, both sheared and massive with ilmenite exsolutions. In the case of banded rocks, this may be due to a later recrystallization at temperatures lower than the worksheet range (~600 °C). The mylonitic fabric in these rocks suggests a shear episode. Since magnetite–ulvöspinel exsolutions are also observed, the subsolvus processes may be post-deformation. The second case (massive with ilmenite exsolutions) is far more complex. According to [70], the Trellis oxy-exsolutions form from an original titaniferous magnetite (Fe_3O_4–Fe_2TiO_{4ss}) which has been partly or almost completely oxidized to produce magnetite + ilmenite ± hematite (Fe_3O_4 + $FeTiO_3$ ± Fe_2O_3), being ilmenite partly or almost completely exsolved within the magnetite as thick lamellae or locally as granules (like in Figure 6n–o). According to [75], this process could take place above or below the magnetite–ulvöspinel solvus, but [70] stated that the oxidation of ulvöspinel occurs above, and [59] explained that this process takes place above 600°C. The Trellis oxy-exsolution, which has been observed only in some samples of Chiange Velho, could tentatively be the result of a different phenomenon such as a thermal aureole of the red granites near the city of Chiange.

The absence of hematite exsolutions and the low hematite component in ilmenite (Figure 10) are coherent with the low oxygen fugacity conditions ($10^{-14.7}$ to $10^{-24.7}$; Figure 11).

5.2. Genesis of the Fe–Ti(–V) Oxide Bodies in the KIC

The genesis of Fe–Ti(–V) oxide mineralisations related to Proterozoic massif-type anorthosite complexes has been explained through a variety of processes: (i) Fractional crystallization coupled with crystal sorting by density [76–79]; (ii) immiscibility between silicate and oxide magmas [80]; (iii) magma mixing [81]; (iv) stress-driven melt segregation [82]; (v) solid-state remobilization [83–86] and (vi) hydrothermal remobilization [87,88].

The formation of the parent magmas for massif-type anorthosites is controversial: Some authors propose that they form after mantle melting [89–91], whereas others point to melting of the mafic lower crust [92–94]. According to [30], it is unlikely that a large volume of calcic plagioclase, like in the KIC, cumulated from crustal melts, which is supported by Sr and Nd isotopic compositions of the anorthosite, which suggest a mantle source. At first, massif-type anorthosites were interpreted to have intruded in the deepest crust [95], but according to [90], there is evidence of shallower emplacements in other localities, such as the Laramie anorthosite in Wyoming [96].

Proterozoic anorthosite massif-type occurrences are interpreted to form from high Al-basalt to jotunite (hypersthene-bearing monzodiorite) magmas, in two stages: (i) Crystallization and accumulation of plagioclase at the top of a deep magma chamber; and (ii) intrusion of plagioclase mushes into the crust. In addition, the foliation observed in many anorthosite complexes, as in the KIC, are described as syn-emplacement features ([6] and references therein). Magmas parental to anorthosites and their residual liquids are TiO_2-enriched (>4 wt % TiO_2), which would promote early saturation of ilmenite, even at high fO_2 [97]. The first minerals to form are plagioclase and ilmenite. The different densities would produce an oxide-enrichment process, leading to the flotation of plagioclase and sinking of ilmenite, and therefore to the concentration of Fe–Ti oxides to form massive bodies [98]. In this case (massive deposits formed by fractional crystallization and separation by density), the Fe–Ti(–V) oxide ore bodies would be concordant with the intrusive anorthosite. However, in some massif-type anorthosite Fe–Ti(–V) oxide deposits worldwide (e.g., Damiao in China, Tellnes in Norway and Lac Tio in Canada), the elongated bodies are discordant (or with intrusive relationships) with the anorthosite hosts [6]. Although the contact between the oxide bodies of the KIC and their hosts could not be determined in the field, layering in the anorthosite is not parallel to the elongation of the massive oxide bodies, so they can be considered discordant (Figure 2a).

In the KIC, reference [30] proposed that partial mantle melts generated at the base of the Congo craton by mantle upwelling and ascended through translithospheric fractures to the crust-mantle boundary. Differentiation of the partial melts occurred and Al-basalt ascended to the crust. During or after this emplacement, draining of the residual liquid produced the massif-type anorthosite. New fractionation of the partial melts produced high Al-basalt intrusion in the massif-type anorthosite as sills, crosscutting and altering the host anorthosite. At this point the complex began to dome, which produced deformation in the solidified sills and draining of liquid in the younger, not yet solidified sills. This draining of liquid would accumulate oxides and sulphides. Later on, mafic-ultramafic bodies intruded through fractures around the anorthosite.

As interpreted by [3], the P_2O_5/TiO_2 versus P_2O_5 trend observed in Figure 3e indicates that both massive ("Fe–Ti ores" in the paper) and nelsonite ("Fe–Ti–P ores") formed from the same nelsonitic magma. This is supported by the homogeneous composition of ilmenite in terms of MgO (geikielite component, Figure 9). In the KIC, nelsonites are irregularly distributed and the variable proportions of apatite preclude a liquid with eutectic composition [12]. This would produce later crystallization of magnetite with relatively high V, like in the Fedorivka layered intrusion (up to 1.85 wt % V; [17]).

In addition, the calculated temperatures and oxygen fugacities overall would suggest that the Fe–Ti(–V) oxide bodies remained long time at a certain depth (8 kbar~24 km), which is consistent with

the KIC being the result of recurrent magmatism that lasted up to 30 My [30], like most massif-type anorthosite complexes [99].

5.3. Massif-Type Anorthosite Fe–Ti(–V) Oxide Bodies in the Angolan KIC and Economic Significance

The Fe–Ti(–V) oxide ore bodies studied from the KIC are constituted by massive, several meters long, lenticular or dike-like bodies composed mostly of Fe–Ti(–V) oxides and lesser amounts (<15 modal %) of other phases (that is to say, with low amounts of impurities). The mineralogy of the studied Fe–Ti(–V) oxide bodies is dominated by titaniferous magnetite, which is consistent with the KIC being a labradorite-type anorthosite [6]. As observed in Figure 3, the KIC contain less TiO_2 than Lac Tio and Tellnes, (which are ilmenite-dominated), and lower Fe/Ti than Lac Tio, because the KIC ore bodies (like Damiao and Tellnes) contain less hematite.

Despite some Fe–Ti(–V) oxide occurrences are small (Dongue Sul, Tchingunguanganda, Tchimbueio), the kilometric length and decametric width of the outcropping Chiange Velho ore body (already stated by [17]) has economic potential for V (contained in magnetite), but especially for Ti, because Chiange Velho is the ore body with the highest ilmenite content of the four studied ore bodies (32–38 modal %).

Massif-type anorthosite Fe–Ti(–V) oxide deposits contain remarkable amounts of V, like the Saint Charles deposit, with 0.1 wt % V_2O_3, and the Buttercup deposit, with 0.67 wt % V_2O_3, both in Québec, Canada [100]. Given the abundance of titaniferous magnetite, the Angolan KIC ore bodies are a potential source of V with an average of 0.27 wt % V_2O_3 in titaniferous magnetite. In addition, despite not being widespread in the KIC, nelsonites could represent a likely resource for P and REE after concentration of apatite, especially in the case of Dongue Sul, where nelsonites contain higher amounts of fluorapatite and are coarser grained.

6. Conclusions and Future Developments

The detailed mineralogical and thermo-oxybarometric characterization of the four Fe–Ti(–V) oxide bodies studied of the Angolan KIC leaded to the following conclusions:

- According to the calculated temperatures and the observed textures, the thermal history and crystallization sequence of the KIC mineralizations included: (1) Crystallization in equilibrium of titaniferous magnetite, ilmenite and spinel below 1300 °C (between 850 °C and 1000 °C in nelsonites); (2) exsolution of aluminous spinel in titaniferous magnetite below 850 °C; (3) shear deformation in Chiange Velho that produced mylonitic fabrics in some rocks and recrystallization below 600 °C; (4) exsolution of titaniferous magnetite in ulvöspinel and magnetite below 450 °C (Figure 12). This suggests that the Fe–Ti(–V) oxide bodies associated to the massif-type anorthosite may have remained long time at a certain depth (8 kbar~24 km).
- The Fe–Ti(–V) oxide bodies of the Angolan KIC contain remarkable reserves of Ti, V, P and REE that may represent an economic resource.

Further work is needed to constrain the tonnage of the deposit. Trace element analyses on titaniferous magnetite and ilmenite from the Fe–Ti(–V) KIC oxide bodies could shed light on element mobility during cooling.

Supplementary Materials: The four tables contained in this article (Tables S1–S4) are available online at www.mdpi.com/2075-163X/7/12/246/s1, Table S1: Whole rock analyses of representative samples of the studied KIC Fe–Ti(–V) oxide bodies, Table S2: Representative EMP analyses of titaniferous magnetite from the four KIC Fe–Ti(–V) oxide bodies studied (in wt %) and the corresponding calculated structural formulae (in a.p.f.u.), Table S3: Representative EMP analyses of ilmenite from the four KIC Fe–Ti(–V) oxide bodies studied (in wt %) and the corresponding calculated structural formulae (in a.p.f.u.), Table S4: Representative EMP analyses of aluminous spinel from the four KIC Fe–Ti(–V) oxide bodies studied (in wt %) and the corresponding calculated structural formulae (in a.p.f.u.).

Acknowledgments: This research was possible thanks to the research projects 2009-SGR-444 and 2014-SGR-1661 of the AGAUR (Generalitat de Catalunya) and to the project CGL2009-13758 (subprogram BTE) of the Spanish

Ministry of Science and Innovation; and to the CCiT-UB, to Eva Prats and Aránzazu Villuendas in particular. The Authors are grateful to Fidel Costa for use of the field-emission electron microprobe in the EOS and to Joaquín A. Proenza for his support during the research. The careful revision of an early and a later version of this manuscript made by Jean Clair Duchesne is sincerely acknowledged, as well as the thorough review made by two anonymous reviewers, which highly improved the quality of the manuscript.

Author Contributions: J.C.M. conceived the ideas for this study; C.V.-d.-B., L.T., M.C.-O., M.C., A.O.G. and J.C.M C.V.B. participated in the field work and sample collection; X.L. designed the strategy for the EMP analyses; C.V.-d.-B., S.G., J.C.M. analyzed and discussed the resulting data; C.V.-d.-B.., L.T., M.C.-O., M.C., X.L., S.G. and J.C.M. wrote the paper.

Conflicts of Interest: The authors declare no conflict of interest.

References

1. Gross, G.A.; Gower, C.F.; Lefebure, D.V. *Magmatic Ti-Fe ± V Oxide Deposits, in: Geological Fieldwork*; Paper 1998-1; British Columbia Ministry of Employment and Investment: Vancouver, BC, Canada, 1997; pp. 24J-1–24J-3.
2. Kesler, S.E.; Simon, A.C. *Mineral Resources, Economics and the Environment*, 2nd ed.; Cambridge University Press: Cambridge, UK, 2015; 446p.
3. Chen, W.T.; Zhou, M.F.; Zhao, T.P. Differentiation of nelsonitic magmas in the formation of the ~1.74 Ga Damaio Fe-Ti-P ore deposit, North China. *Contrib. Mineral. Petrol.* **2013**, *165*, 1341–1362. [CrossRef]
4. Polyak, D.E. USGS Mineral Commodity Summaries, Vanadium. Available online: https://minerals.usgs.gov/minerals/pubs/commodity/vanadium/mcs-2017-vanad.pdf (accessed on 13 December 2017).
5. Zhou, M.F.; Chen, W.T.; Wang, C.Y.; Prevec, S.A.; Liu, P.P.; Howarth, G.H. Two stages of immiscible liquid separation in the formation of Panzhihua-type Fe-Ti-V oxide deposits, SW China. *Geosci. Front.* **2013**, *4*, 481–502. [CrossRef]
6. Charlier, B.; Namur, O.; Bolle, O.; Latypov, R.; Duchesne, J.C. Fe-Ti-V-P ore deposits associated with Proterozoic massif-type anorthosites and related rocks. *Earth Sci. Rev.* **2015**, *141*, 56–81. [CrossRef]
7. Hébert, C.; Cadieux, A.M.; van Breemen, O. Temporal evolution and nature of Ti-Fe-P mineralization in the anorthosite-mangerite-charnockite-granite (AMCG) suites of the south-central Grenville Province, Saguenay-Lac St. Jean area, Quebec, Canada. *Can. J. Earth Sci.* **2005**, *42*, 1865–1880. [CrossRef]
8. Ashwal, L.D.; Twist, D. The Kunene complex, Angola/Namibia: A composite massif-type anorthosite complex. *Geol. Mag.* **1994**, *131*, 579–591. [CrossRef]
9. Mayer, A.; Hofmann, A.W.; Sinigoi, S.; Morais, E. Mesoproterozoic Sm–Nd and U–Pb ages for the Kunene Anorthosite Complex of SW Angola. *Precambrian Res.* **2004**, *133*, 187–206. [CrossRef]
10. Menge, G.F.W. The antiformal structure and general aspects of the Kunene Complex. *Z. Dtsch. Geol. Ges.* **1998**, *149*, 431–448.
11. Drüppel, K.; Von Seckendorff, V.; Okrusch, M. Subsolidus reaction textures in the anorthositic rocks of the southern part of the Kunene Intrusive Complex, NW Namibia. *Eur. J. Mineral.* **2001**, *13*, 289–309. [CrossRef]
12. Drüppel, K.; Littmann, R.L.; Romer, R.L.; Okrusch, M. Petrology and isotope geochemistry of the Mesoproterozoic anorthosite and related rocks of the Kunene Intrusive Complex, NW Namibia. *Precambrian Res.* **2007**, *156*, 1–31. [CrossRef]
13. Gleißner, P.; Drüppel, K.; Taubald, H. Magmatic evolution of anorthosites of the Kunene Intrusive Complex, NW Namibia: Evidence from oxygen isotope data and trace element zoning. *J. Petrol.* **2010**, *51*, 897–919. [CrossRef]
14. Morais, E.; Sinigoi, S.; Mayer, A.; Mucana, A.; Miguel, L.G.; Rufino Neto, J. The Kunene gabbro-anorthosite Complex: Preliminary results based on new field and chemical data. *Afr. Geosci. Rev.* **1998**, *5*, 485–498.
15. Cardoso, S.M.; Marques, J.M. *Notícia Explicativa da Folha n° 378 (Chibemba), Carta Geológica de Angola—Escala 1:100,000*; Direcção Provincial dos Serviços de Geologia e Minas de Angola: Luanda, Angola, 1971.
16. De Carvalho, H. *Notícia Explicativa da Folha n° 377 (Vila de Almoster), Carta Geológica de Angola—Escala 1:100,000*; Direcção Provincial dos Serviços de Geologia e Minas de Angola: Luanda, Angola, 1972.
17. Lorena, S.A.P. Ocorrências de ilmenites no sul de Angola. *Bol. Serv. Geol. Minas Angola* **1969**, *20*, 21–23.
18. De Carvalho, H.; Alves, P.H. *Gabbro-Anorthosite Complex of SW Angola/NW Namibia*; Serie de Ciencias da Terra; Comunicações Instituto Investigação Científica Tropical: Lisboa, Portugal, 1990; pp. 5–64.

19. De Carvalho, H.; Alves, P.H. *The Precambrian of SW Angola and NW Namibia*; General Remarks, Correlation Analysis, Economic Geology; Comunicações Instituto Investigação Científica Tropical: Lisboa, Portugal, 1993; Volume 4, p. 38.
20. De Carvalho, H.; Tassinari, C.; Alves, P.H.; Guimarães, F.; Simões, M.C. Geochronological review of the Precambrian in western Angola: Links with Brazil. *J. Afr. Earth Sci.* **2000**, *31*, 383–402. [CrossRef]
21. Silva, Z.C.G. Geochemistry of the gabbro-anorthosite Complex of Angola. *J. Afr. Earth Sci.* **1990**, *10*, 683–692. [CrossRef]
22. Silva, Z.C.G. Mineralogy and cryptic layering of the Kunene anorthosite complex of SW Angola and Namibia. *Mineral. Mag.* **1992**, *56*, 319–327. [CrossRef]
23. Ramdohr, P. Ulvöspinel and its significance in titaniferous iron ores. *Econ. Geol.* **1953**, *48*, 677–688. [CrossRef]
24. Simpson, E.S.W. The anorthosite of southern Angola: A review of present data. In *African Magmatism and Tectonics*; Clifford, T.N., Gass, I.G., Eds.; Oliver and Boyd: Edinburgh, UK, 1970; pp. 89–96.
25. Roman'ko, E.F.; Titov, V.I. Iron-titanium ore mineralization in the Kunene intrusive massif. *Izv. Vyssh. Uchebn. Zaved. Geol. Razved.* **2005**, *6*, 35–38.
26. Simpson, E.S.W.; Otto, J.D.T. On the Precambrian anorthosite mass of southern Angola. In Proceedings of the 21st International Geological Congress; Det Berlingske Bogtrykkeri: Copenhagen, Denmark, 1960; Volume 13, pp. 216–227.
27. Vermaak, C.F. Kunene Anorthosite Complex. In *Precambrian of the Southern Hemisphere, Developments in Precambrian Geology*; Hunter, D.R., Ed.; Elsevier: Amsterdam, The Netherlands, 1981; Volume 2, pp. 578–599, ISBN 0444418628.
28. Stone, P.; Brown, G.M. The Quihita-Cunene layered gabbroic intrusion of South-West Angola. *Geol. Mag.* **1958**, *95*, 195–206. [CrossRef]
29. Slejko, F.; Demarchi, G.; Morais, E. Mineral chemistry and Nd isotopic composition of two anorthositic rocks from the Kunene Complex (SW Angola). *J. Afr. Earth Sci.* **2002**, *35*, 77–88. [CrossRef]
30. Maier, W.D.; Rasmussen, B.; Fletcher, I.R.; Li, C.; Barnes, S.-J.; Huhma, H. The Kunene anorthosite complex, Namibia, and its satellite intrusions: Geochemistry, geochronology, and economic potential. *Econ. Geol.* **2013**, *108*, 953–986. [CrossRef]
31. Brandt, S.; Klemd, R.; Okrusch, M. Ultrahigh-Temperature Metamorphism and Multistage Evolution of Garnet–Orthopyroxene Granulites from the Proterozoic Epupa Complex, NW Namibia. *J. Petrol.* **2003**, *44*, 1121–1144. [CrossRef]
32. Brandt, S.; Klemd, R. Upper-amphibolite facies partial melting of paragneisses from the Epupa Complex, NW Namibia, and relations to Mesoproterozoic anorthosite magmatism. *J. Metamorph. Geol.* **2008**, *26*, 871–893. [CrossRef]
33. Seth, B.; Armstrong, R.A.; Brandt, S.; Villa, I.M.; Kramers, J.D. Mesoproterozoic U-Pb and Pb-Pb ages of granulites in NW Namibia: Reconstructing a complete orogenic cycle. *Precambrian Res.* **2003**, *126*, 147–168. [CrossRef]
34. Seth, B.; Armstrong, R.A.; Büttner, A.; Villa, I.M. Time constraints for Mesoproterozoic upper amphibolite facies metamorphism in NW Namibia: A multi-isotopic approach. *Earth Planet. Sci. Lett.* **2005**, *230*, 355–378. [CrossRef]
35. Kröner, A.; Rojas-Agramonte, Y.; Wong, J.; Wilde, S.A. Zircon reconnaissance dating of Proterozoic gneisses along the Kunene River of Northwestern Namibia. *Tectonophysics* **2015**, *662*, 125–139. [CrossRef]
36. Torquato, J.R.; Silva, A.T.S.F.; da Cordani, U.G.; Kawashita, K. A evolução geológica do Cinturão Móvel do Quipungo no Ocidente de Angola. *An. Acad. Brasil. Geocienc.* **1979**, *51*, 133–143.
37. De Carvalho, H.; Fernandez, A.; Vialette, Y. Chronologie absolue du Précambrien du Sud-Ouest de l'Angola. *C. R. Acad. Sci. Paris* **1979**, *288*, 1647–1650.
38. Maier, W.D.; Teigler, B.; Miller, R. The Kunene anorthosite complex and its satellite intrusions. In *The Geology of Namibia*; Miller, R.M.G., Ed.; Geological Survey of Namibia: Windhoek, Namibia, 2008; pp. 9-1–9-18, ISBN 9780869767313.
39. Mayer, A.; Sinigoi, S.; Miguel, L.G.; Morais, E.; Petrini, R. Kibaran ages in the Kunene anorthositic complex. *Abstr. Geoluanda* **2000**, 106.
40. Morais, E.; Sinigoi, S.; Mayer, A.; Miguel, L.G. The Kunene gabbro-anorthosite Complex: Coalescence of discrete crystal mush intrusions. *Abstr. Geoluanda* **2000**, 110.

41. Drüppel, K.; Okrusch, M. Geo-und isotopenchemische Untersuchungen der Anorthosite des Kunene-Intrusiv-Komplexes (KIC) in NW-Namibia. *Eur. J. Mineral.* **2000**, *12*, 37.
42. Bassot, J.P.; Pascal, M.; Vialette, Y. Données nouvelles sur la stratigraphie, la géochemie et la géochronologie des formations precambriennes de la partie meridionale du Haut Plateau angolais. *Bull. BRGM sec 4 Géol. Gén.* **1981**, *4*, 285–309.
43. De Carvalho, H.; Crasto, J.; Silva, Z.C.; Vialette, Y. The Kibaran cycle in Angola: A discussion. *Afr. Geol. Rev. Geol. J.* **1987**, *22*, 85–102. [CrossRef]
44. Von Seckendorff, V.; Drüppel, K.; Okrusch, M.; Littmann, S.; Cook, N. Oxide-sulphide relationships in sodalite-bearing metasomatites of the Empembe-Swartbooisdrif Alkaline Province, North-West Namibia. *Miner. Deposita* **2000**, *35*, 430–450. [CrossRef]
45. Franke, H.; Drüppel, K.; Brätz, H. Formation of anorthosite-related Fe-Ti deposits, Namibia. *Geochim. Cosmochim. Acta* **2009**, *73* (Suppl. 1), A394.
46. Gleißner, P.; Drüppel, K.; Becker, H. Osmium isotopes and highly siderophile element fractionation in the massif-type anorthosites of the Mesoproterozoic Kunene Intrusive Complex, NW Namibia. *Chem. Geol.* **2012**, *302–303*, 33–47. [CrossRef]
47. Pouchou, J.L.; Pichoir, F. Quantitative analysis of homogeneous or stratified microvolumes applying the model PAP. In *Electron Probe Quantitation*; Heinrich, K.J., Newbury, D.E., Eds.; Plenum Press: New York, NY, USA, 1991; pp. 31–75, ISBN 978-1-4899-2619-7.
48. Carmichael, I.S.E. The iron-titanium oxides of salic volcanic rocks and their associated ferromagnesian silicates. *Contrib. Mineral. Petrol.* **1967**, *14*, 36–64. [CrossRef]
49. Torres Roldán, R.L.; García-Casco, A.; García-Sánchez, P.A. CSpace: An integrated workplace for the graphical and algebraic analysis of phase assemblages on 32-bit Wintel platforms. *Comput. Geosci.* **2000**, *26*, 779–793. [CrossRef]
50. Whitney, D.L.; Evans, B.W. Abbreviations for names of rock-forming minerals. *Am. Mineral.* **2010**, *95*, 185–187. [CrossRef]
51. Villanova-de-Benavent, C.; Galí, S.; Melgarejo, J.C.; Gonçalves, A.O. Fe-Ti(-V) oxide mineralogy and thermo-oxybarometry from the Kunene anorthosite Complex deposits (SW Angola). In *Let's Talk Ore Deposits: Proceedings of the 11th Biennial SGA Meeting*; Barra, F., Reich, M., Campos, E., Tornos, F., Eds.; Universidad Católica del Norte: Antofagasta, Chile, 2011; pp. 465–467, ISBN 9789562873291.
52. Zhao, T.P.; Chen, W.; Zhou, M.F. Geochemical and Nd-Hf isotopic constraints on the origin of the ~1.74-Ga Damiao anorthosite complex, North Xina Craton. *Lithos* **2009**, *113*, 673–690. [CrossRef]
53. Zhou, M.F.; Robinson, P.T.; Lesher, C.M.; Keays, R.R.; Zhang, C.J.; Malpas, J. Geochemistry, petrogenesis and metallogenesis of the Panzhihua gabbroic layered intrusion and associated Fe-Ti-V oxide deposits, Sichuan Province, SW China. *J. Petrol.* **2005**, *46*, 2253–2280. [CrossRef]
54. Duchesne, J.C.; Liégeois, J.P. The origin of nelsonite and high-Zr ferrodiorite associated with Proterozoic anorthosite. *Ore Geol. Rev.* **2015**, *71*, 40–56. [CrossRef]
55. Zhou, M.-F.; Arndt, N.T.; Malpas, J.; Wang, C.Y.; Kennedy, A.K. Two magma series and associated ore deposit types in the Permian Emeishan large igneous province, SW China. *Lithos* **2008**, *103*, 352–368. [CrossRef]
56. Charlier, B.; Sakoma, E.; Sauvé, M.; Stanaway, K.; Vander Auwera, J.; Duchesne, J.C. The Grader layered intrusion (Havre-Saint Pierre anorthosite, Quebec) and genesis of nelsonite and other Fe-Ti-P ores. *Lithos* **2008**, *101*, 359–378. [CrossRef]
57. Waychunas, G.A. Crystal chemistry of oxides and oxyhydroxides. In *Oxide Minerals: Petrologic and Magnetic Significance*; Lindsley, D.H., Ed.; Mineralogical Society of America: Chantilly, VA, USA, 1991; Volume 25, pp. 11–68, ISBN 0-939950-30-8.
58. McDonough, W.F.; Sun, S.S. The composition of the Earth. *Chem. Geol.* **1995**, *120*, 223–253. [CrossRef]
59. Haggerty, S.E. Oxide textures-a mini atlas. *Rev. Mineral.* **1991**, *25*, 303–321.
60. Duchesne, J.C. Iron-titanium oxide minerals in the Bjerkrem-Sokndal Massif, South-western Norway. *J. Petrol.* **1972**, *13*, 57–81. [CrossRef]
61. Von Gruenewaldt, G.; Klemm, D.D.; Henckel, J.; Dehm, R.M. Exolution features in titanomagnetites from massive magnetite layers and their host rocks of the Upper Zone, Eastern Bushveld Complex. *Econ. Geol.* **1985**, *80*, 1041–1061. [CrossRef]

62. Ivanyuk, G.Y.; Kalashnikov, A.O.; Pakhomovsky, Y.A.; Bazai, A.V.; Goryainov, P.M.; Mikhailova, J.A.; Yakovenchuk, V.N.; Konopleva, N.G. Subsolidus Evolution of the Magnetite-Spinel-Ulvöspinel Solid Solutions in the Kovdor Phoscorite-Carbonatite Complex, NW Russia. *Minerals* **2017**, *7*, 215. [CrossRef]
63. Duchesne, J.C. Les gisements d'oxydes de fer et titane dans les roches anorthositiques du Rogaland (Norvège méridionale). *Colloq. Sci. Int. Eugène Raguin* **1973**, 241–248.
64. Sauerzapf, U.; Lattard, D.; Burchard, M.; Engelmann, R. The titanomagnetite-ilmenite equilibrium: New experimental data and thermo-oxybarometric application to the crystallization of basic to intermediate rocks. *J. Petrol.* **2008**, *49*, 1161–1185. [CrossRef]
65. Spencer, K.J.; Lindsley, D.H. A solution model for coexisting iron-titanium oxides. *Am. Mineral.* **1981**, *66*, 1189–1201.
66. Lister, G.F. The composition and origin of selected iron-titanium deposits. *Econ. Geol.* **1966**, *61*, 275–310. [CrossRef]
67. Buddington, A.F.; Lindsley, D.H. Iron-titanium oxide minerals and their synthetic equivalents. *J. Petrol.* **1964**, *5*, 310–357. [CrossRef]
68. Frost, B.R. Introduction to oxygen fugacity and its petrologic importance. *Rev. Mineral. Geochem.* **1991**, *25*, 303–321.
69. Jakobsson, S.; Oskarsson, N. The system C-O in equilibrium with graphite at high pressure and temperature: An experimental study. *Geochim. Cosmochim. Acta* **1994**, *58*, 9–17. [CrossRef]
70. Duchesne, J.C. Microstructures of Fe-Ti oxide minerals in the South Rogaland anorthositic complex (Norway). *Ann. Soc. Geol. Belg.* **1970**, *93*, 527–544.
71. Price, G.D. Subsolidus phase relations in the titanomagnetite solid solution series. *Am. Mineral.* **1981**, *66*, 751–758.
72. Haggerty, S.E. Oxidation of opaque mineral oxides in basalts. In *Oxide Minerals*; Rumble, D., Ed.; Mineralogical Society of America: Chantilly, VA, USA, 1976; Volume 3, pp. Hg1–Hg100, ISBN 0-939950-03-0.
73. Haggerty, S.E. Opaque mineral oxides in terrestrial igneous rocks. In *Oxide Minerals*; Rumble, D., Ed.; Mineralogical Society of America: Chantilly, VA, USA, 1976; Volume 3, pp. Hg101–Hg300, ISBN 0-939950-03-0.
74. Turnock, A.C.; Eugster, H.P. Fe-Al oxides: Phase relationships below 1000 °C. *J. Petrol.* **1962**, *3*, 533–565. [CrossRef]
75. Vincent, E.A. Ulvöspinel in the Skaergaard intrusion, East Greenland. *Neues Jahrb. Mineral. Abh.* **1960**, *94*, 992–1016.
76. Morse, S.A. The feldspar/magma density paradox. In *The Nain Anorthosite Project, Labrador: Field Report 1971*; Morse, S.A., Ed.; University of Massachusetts at Amherst: Amherst, MA, USA, 1971; Volume 9, pp. 113–116.
77. Campbell, I.H.; Roeder, P.L.; Dixon, J.M. Plagioclase buoyancy in basaltic liquids as determined with a centrifuge furnace. *Contrib. Mineral. Petrol.* **1978**, *67*, 369–377. [CrossRef]
78. Scoates, J.S. The plagioclase-magma density paradox re-examined and the crystallization of Proterozoic anorthosites. *J. Petrol.* **2000**, *41*, 627–649. [CrossRef]
79. Charlier, B.; Duchesne, J.C.; Vander Auwera, J. Magma chamber processes in the Tellnes ilmenite deposit (Rogaland anorthosite province; SW Norway) and the formation of Fe-Ti ores in massif-type anorthosites. *Chem. Geol.* **2006**, *234*, 264–290. [CrossRef]
80. Philpotts, A.R. Origin of certain iron-titanium oxide and apatite rocks. *Econ. Geol.* **1967**, *62*, 303–315. [CrossRef]
81. Charlier, B.; Namur, O.; Malpas, S.; De Marneffe, C.; Duchesne, J.C.; Vander Auwera, J.; Bolle, O. Origin of the giant Allard Lake ilmenite ore deposit (Canada) by fractional crystallization, multiple magma pulses and mixing. *Lithos* **2010**, *117*, 119–134. [CrossRef]
82. Kohlstedt, D.L.; Zimmerman, M.E.; Mackwell, S.J. Stress-driven melt segregation in partially molten feldspathic rocks. *J. Petrol.* **2010**, *51*, 9–19. [CrossRef]
83. Paludan, J.; Hansen, U.B.; Olesen, N.Ø. Structural evolution of the Precambrian Bjerkreim–Sokndal intrusion, South Norway. *Nor. Geol. Tidsskr.* **1994**, *74*, 185–198.
84. Wilson, J.R.; Robins, B.; Nielsen, F.; Duchesne, J.C.; Vander Auwera, J. The Bjerkreim-Sokndal layered intrusion, Southwest Norway. In *Layered Intrusions*; Cawthorn, R.G., Ed.; Elsevier: Amsterdam, The Netherlands, 1996; pp. 231–256, ISBN 0444540644.

85. Duchesne, J.C. Liquid ilmenite or liquidus ilmenite: A comment on the nature of ilmenite vein deposits. In *Petrology and Geochemistry of Magmatic Suites of Rocks in the Continental and Oceanic Crusts (a Volume Dedicated to Professor Jean Michot)*; Demaiffe, D., Ed.; Royal Museum for Central Africa: Tervuren, Belgium; Université Libre de Bruxelles: Bruxelles, Belgium, 1996; pp. 73–82.
86. Duchesne, J.C.; Shumlyanskyy, L.; Charlier, B. The Fedorivka layered intrusion (Korosten Pluton, Ukraine): An example of highly differentiated ferrobasaltic evolution. *Lithos* **2006**, *89*, 353–376. [CrossRef]
87. Li, L.; Li, H.; Chen, Z.; Wang, D.; Chen, W. Hydrothermal mineralization and fluid inclusion study on the Heishan iron deposit, Chengde County, Hebei Province, China. *Acta Petrol. Sin.* **2010**, *26*, 858–870.
88. Li, H.; Li, L.; Zhang, Z.; Santosh, M.; Liu, M.; Cui, Y.; Yang, X.; Chen, J.; Yao, T. Alteration of the Damiao anorthosite complex in the northern North China Craton: Implications for high-grade iron mineralization. *Ore Geol. Rev.* **2014**, *57*, 574–588. [CrossRef]
89. Emslie, R.F. Anorthosite massifs, rapakivi granites and late Proterozoic rifting of North America. *Precambrian Res.* **1978**, *7*, 61–98. [CrossRef]
90. Ashwal, L.D. *Anorthosites*; Springer-Verlag: Berlin, Germany, 1993; ISBN 978-3-642-77442-3.
91. Bybee, G.M.; Ashwal, L.D.; Shirey, S.B.; Horan, M.; Mock, T.; Andersen, T.B. Pyroxene megacrysts in Proterozoic anorthosites: Implications for tectonic setting, magma source and magmatic processes at the Moho. *Earth Planet. Sci. Lett.* **2014**, *389*, 74–85. [CrossRef]
92. Duchesne, J.C. Fe–Ti deposits in Rogaland anorthosites (South Norway): Geochemical characteristics and problems of interpretation. *Miner. Deposita* **1999**, *34*, 182–198. [CrossRef]
93. Longhi, J. A mantle or mafic crustal source for Proterozoic anorthosites? *Lithos* **2005**, *83*, 183–198. [CrossRef]
94. Longhi, J.; Vander Auwera, J.; Fram, M.S.; Duchesne, J.C. Some phase equilibrium constraints on the origin of Proterozoic (massif) anorthosites and related rocks. *J. Petrol.* **1999**, *40*, 339–362. [CrossRef]
95. Martignole, J.; Schrijver, K. The level of anorthosites and its tectonic pattern. *Tectonophysics* **1970**, *10*, 403–409. [CrossRef]
96. Kolker, A.; Lindsley, D.H. Geochemical evolution of the Maloin Ranch pluton, Laramie Anorthosite Complex, Wyoming: Petrology and mixing relations. *Am. Mineral.* **1989**, *74*, 307–324.
97. Toplis, M.J.; Carroll, M.R. An experimental study of the influence of oxygen fugacity on Fe–Ti oxide stability, phase relations, and mineral-melt equilibria in ferro-basaltic systems. *J. Petrol.* **1995**, *36*, 1137–1170. [CrossRef]
98. Vander Auwera, J.; Longhi, J. Experimental study of a jotunite (hypersthene monzodiorite): Constraints on the parent magma composition and crystallization conditions (P, T, fO_2) of the Bjerkreim-Sokndal layered intrusion (Norway). *Contrib. Mineral. Petrol.* **1994**, *118*, 60–78. [CrossRef]
99. Frost, C.D.; Chamberlain, K.R.; Frost, K.R.; Scoates, J.R. The 1.76 Ga Horse Creek anorthosite complex, Wyoming: A massif anorthosite emplaced late in the Medicine Bow orogeny. *Rocky Mt. Geol.* **2000**, *35*, 71–90. [CrossRef]
100. Corriveau, L.; Perreault, S.; Davidson, A. Prospective metallogenic settings of the Grenville Province. In *Mineral Deposits of Canada: A Synthesis of Major Deposit-Types, District Metallogeny, The Evolution of Geological Provinces, and Exploration Methods*; Goodfellow, W.D., Ed.; Mineral Deposits Division, Geological Survey of Canada: Ottawa, ON, Canada, 2007; pp. 819–847.